Mechanical activation of TWIK-related potassium channel by nanoscopic movement and rapid second messenger signaling.

E. Nicholas Petersen[1,4], Mahmud Arif Pavel[1], Samuel S. Hansen[1], Manasa Gudheti[5], Hao Wang[1,4], Zixuan Yuan[1,4], Keith R. Murphy[2,3], William W. Ja[2,3], Heather A Ferris[5], Erik M. Jorgensen[6], Scott B. Hansen[1]

[1]Departments of Molecular Medicine, [2]Department of Neuroscience, [3]Center on Aging, [4]Scripps Research Skaggs Graduate School of Chemical and Biological Science, The Scripps Research Institute, Scripps, Florida 33458, USA

[5]Division of Endocrinology and Metabolism, [5]Center for Brain Immunology and Glia, Department of Neuroscience, University of Virginia, Charlottesville, VA 22908, USA

[6]Department of Biology, Howard Hughes Medical Institute, University of Utah, Salt Lake City, UT 84112, USA

*Correspondence: shansen@scripps.edu

Summary: Shear thinning activates TREK-1 through a second messenger.

Abstract

Rapid conversion of force into a biological signal enables living cells to respond to mechanical forces in their environment. The force is believed to initially affect the plasma membrane and then alter the behavior of membrane proteins. Phospholipase D2 (PLD2) is a mechanosensitive enzyme that is regulated by a structured membrane-lipid site comprised of cholesterol and saturated ganglioside (GM1). Here we show stretch activation of TWIK-related K^+ channel (TREK-1) is mechanically evoked by PLD2 and spatial patterning involving ordered GM1 and 4,5-

bisphosphate (PIP_2) clusters. First, mechanical force deforms the ordered lipids, which lowers membrane cholesterol, disrupts the interaction of PLD2 with the GM1 lipids, and allows a complex of TREK-1 and PLD2 to associate with PIP_2 clusters. The association with PIP_2 activates the enzyme, which produces the second messenger phosphatidic acid (PA) that gates the channel. Co-expression of catalytically inactive PLD2 inhibits TREK-1 stretch currents in a biological membrane. Cellular uptake of cholesterol inhibits TREK-1 currents in culture and depletion of cholesterol from astrocytes releases TREK-1 from GM1 lipids in mouse brain. Depletion of the PLD2 ortholog in flies results in hypersensitivity to mechanical force. We conclude PLD2 mechanosensitivity combines with TREK-1 ion permeability to elicit a mechanically evoked response.

Keywords: lipid raft; signaling lipid; phospholipase D; mechanosensation; shear thinning

Introduction

All cells respond to mechanical force, a phenomenon known as mechanosensation (Hahn and Schwartz, 2009; Julius, 2001; Ranade et al., 2015). Mechanosensation requires the dual processes of sensing and transducing mechanical force into signals that cells can interpret and respond to. Ion channels serve as one type of transducer. While certain channels have been demonstrated to directly respond to mechanical force in purified lipid environments (Brohawn, 2015; Cox et al., 2019; Teng et al., 2015), others, such as TRP channels, can be downstream components of multi-step signaling cascades (Kwon et al., 2023; Wilde et al., 2022) in cellular membranes, including those involving mechanosensitive G-protein coupled receptors (GPCRs) (Gudi et al., 1998; Lin et al., 2022; Storch et al., 2012; Wei et al., 2018; Xu et al., 2018),.

One of these channels is TWIK-related K^+ channel subtype 1 (TREK-1), a mechanosensitive member of the two-pore-domain potassium (K2P) family known for its analgesic properties. TREK-1 plays a role in inhibiting neuronal firing and reducing pain through

the release of potassium ions (Honoré, 2007). Intriguingly, the enzyme phospholipase D2 (PLD2) directly interacts with the C-terminus of TREK-1, activating the channel by locally producing phosphatidic acid (PA) (Comoglio et al., 2014).

Despite lacking a transmembrane domain, PLD2 exhibits mechanosensitivity (Pavel et al., 2020; Petersen et al., 2016). This property arises from mechanically induced changes in spatial organization of the plasma membrane. Palmitoylations of cysteine residues near its pleckstrin homology (PH) domain, enables PLD2 to bind to a specific site composed of monosialotetrahexosylganglioside (GM1) lipids and cholesterol in the liquid ordered (L_o) region of the membrane (McDermott et al., 2004; Yuan and Hansen, 2023) (Supplemental Fig. S1a-b). Anesthetics compete with palmitates at this site which we call an anesthetic-palmitate (AP) site (Call et al., 2023). Application of mechanical force disrupts the AP site, releasing the palmitates of PLD2 and allowing the PH domain to interact with phosphatidylinositol 4,5-bisphosphate (PIP_2) clusters in the liquid disordered (L_d) region of the membrane (Petersen et al., 2016). This, in turn, triggers enzyme activation through spatial redistribution and substrate presentation (Petersen et al., 2020) (Supplemental Fig. S1c).

Notably, the C-terminus responsible for binding PLD2 is essential for TREK-1 mechanosensitivity in cellular membranes (Brohawn, 2015; Chemin et al., 2007a; Patel et al., 1998). Our previous studies showed the same C-terminus is essential for binding PLD2 during anesthetic activation of TREK-1. In that system, the anesthetic-induced release of PLD2 from GM1 lipids was responsible for all the TREK-1 current evoked by anesthetic in HEK293T cells (Pavel et al., 2020). These results prompted us to investigate whether PLD2's mechanical activation in HEK293T cells contributes to a mechanically evoked TREK-1 current. Analogous to our study on TREK-1 anesthetic sensitivity, here we show that the catalytic activity of PLD2 is indispensable for the generation of mechanically evoked TREK-1 currents in cultured HEK293T cellular membranes. We further show these PLD2-dependent TREK-1 currents result from the

spatial patterning of the channel and enzyme within lipid nanodomains in HEK, N2a, C2C12, and primary neurons. In neurons, this regulatory process is influenced by astrocyte-derived cholesterol.

Results

Dependence on PLD2 for TREK-1 activation.

To assess the involvement of PLD2 mechanosensitivity to a mechanically evoked current from TREK-1 channels, we conducted pressure current measurements in HEK293T cells both with and without the expression of a catalytically inactive K758R PLD2 mutant (xPLD2) (Toschi et al., 2009). We selected HEK293T cells for this study due to their minimal endogenous potassium currents, which allowed us to attribute the recorded currents specifically to TREK-1. The expression of TREK-1 was tracked using an EGFP tag attached to the channels C-terminus, and we confirmed successful expression of all constructs, observing their presence on the cell surface (Fig. S2A-B).

In intact HEK293T cells, the overexpression of xPLD2 substantially inhibited nearly all mechanically evoked TREK-1 currents (Fig. 1A-C). When currents were measured in the inside out configuration under negative pressure conditions (from 0 to -60 mmHg), they exhibited a reduction of over 80% from 0.181 ± 0.04 to 0.035 ± 0.013 pA/μm^2, despite an overall increase in the total levels of TREK-1 (Fig. S2B-C). This observation suggests that if the effect is through a specific PLD2-TREK-1 interaction, then removal of the PLD2 binding domain should also inhibit PLD2-evoked currents.

To investigate further, we eliminated the putative PLD2 binding site on TREK-1 by truncating the C-terminus at residue 322 (TREK trunc) (see Fig. S3A). The pressure induced current in TREK trunc decreased by more than 85%, measuring 0.025 ± 0.013 pA/μm^2 (Fig. 1C

and Fig. S3B). Remarkably, this reduction was nearly identical to the results obtained when full-length TREK-1 (TREK FL) was expressed in conjunction with xPLD2. Importantly, previous studies have confirmed the functionality and mechanosensitivity of this similar truncated TREK-1 when reconstituted into crude soy PC lipids(Stephen G Brohawn et al., 2014).

Conversely, the overexpression of TREK-1 with wild-type (WT) mouse PLD2 (mPLD2) resulted in a substantial augmentation of TREK-1 pressure-dependent currents within HEK293T cells (Fig. 1A, see Supplemental Fig. S3B for raw traces). The TREK-1-evoked currents were markedly significant, both with and without overexpression of mPLD2, when compared to xPLD2 ($p<0.002$ and 0.007 respectively; Fig. 1C). HEK293T cells, like all cells, have endogenous PLD2 (enPLD2). The xPLD2 expression is >10x the endogenous PLD2 (enPLD2) which we previously showed outcompetes the binding of enPLD2 to TREK-1 under similar conditions (Pavel et al., 2020).

The threshold for PLD2-dependent TREK-1 activation proved to be quite sensitive. TREK-1 exhibited responsiveness to negative pressure (ranging from 0 to -60 mmHg, in a non-saturating regime) with a half maximal pressure requirement of approximately 32 mmHg. This pressure led to the generation of up to 200 pA of TREK-1 current (Fig. 1A and Supplemental Fig. S3C), aligning with findings from prior investigations (Stephen G Brohawn et al., 2014; Patel et al., 1998).

As previously mentioned, previous studies demonstrated TREK-1 direct sensitivity to mechanical force in purified lipids, independent of PLD2 (Berrier et al., 2013; Stephen G Brohawn et al., 2014). To delineate a PLD2-independent (i.e., direct) component of TREK-1 mechanotransduction within a cellular membrane we conducted a comparative analysis between cells expressing TREK trunc and mock transfected HEK293T cells (lacking TREK-1 expression). Our results demonstrated that TREK trunc exhibited a modest increase in current, measuring 0.046 ± 0.023 pA/μm^2 ($p=0.08$, Fig. 1c inset), when compared to the condition with no TREK-1. Similarly, in cells expressing xPLD2 alongside full-length TREK-1, the channel exhibited a small

increase in current measuring 0.060 ± 0.035 pA/μm^2 (p=0.11). This PLD2 independent current aligns with direct mechanical activation of TREK-1 observed in liposomes. However, it is important to note that we cannot rule out the possibility of other contributing mechanisms.

Due to the minimal pressure-activated TREK-1 current observed in the presence of xPLD2, we conducted control experiments to validate the presence of functional TREK-1 on the plasma membrane—channels capable of conducting current. TREK-1 is a potassium leak channel with inherent basal currents in cultured cells (Comoglio et al., 2014). It is reasonable to assume that the basal current arises from the presence of basal levels of anionic lipids in the cellular membrane.

As anticipated, we observed TREK-1 basal current both in the presence (16.9 ± 4.3pA/pF) and absences (24.0 ± 4.2 pA/pF) of xPLD2 (Comoglio et al., 2014) (Fig. 1d). These basal resting currents were recorded at 0 mV in HEK293T cells over expressing TREK-1 FL with and without xPLD2. Notably, the current in the presence of xPLD2 was significantly higher than that observed in a nonfunctional control TREK-1 (xTREK), which we previously determined to exhibit no measurable current in unrelated studies. These controls affirm that TREK-1 FL is expressed and functionally active in the presence of xPLD2. Moreover, they highlight the essential role of PLD2 in pressure-activated currents (Fig. 1c), contrasting with the basal leak currents (Fig. 1D; TREK FL, grey bar vs. +xPLD2, red bar), which did not necessitate PLD2.

Mechanical activation of TREK-1 by movement between nanodomains.

As previously reported in a prior publication, we proposed that fluid shear induces the disassociation of PLD2 with cholesterol dependent GM1 clusters and the association with PIP_2 clusters, leading to a change in spatial organization and activation of the enzyme (Fig. S1) (Petersen et al., 2016). Given that TREK-1 binds to PLD2, we hypothesized the channel could undergo a similar mechanically induced spatial reorganization between GM1 and PIP_2 clusters.

To visualize this spatial patterning of TREK-1 in response to shear forces, we developed a method to chemically fix membranes during shear (Fig. 2A). In our experiments, we employed cultured HEK293T cells expressing both TREK-1 and mPLD, which matched the conditions used in our electrophysiology experiments. These cells were subjected to shear forces of 3 dynes/cm^2, a physiologically relevant force to cells (Petersen et al., 2016; Schneck, 1992), using a rotary shear approach. Subsequently, the cells were fixed and labeled for two- or three-color dSTORM. TREK-1 proteins were tagged with EGFP, leveraging its inherent self-blinking properties for detection (Call et al., 2023). Lipids were labeled using Alexa 647 (A647) anti-PIP_2 antibodies or A647-labeled cholera toxin B (CTxB), which selectively bind to PIP_2 and GM1 clusters, respectively (Petersen et al., 2016). By concurrently labeling both lipids and proteins, we were able to monitor the dynamic changes in spatial organization within nanoscopic lipid domains (Yuan and Hansen, 2023). To access the PIP_2 domains on the inner leaflet, cells were permeabilized (see methods). The effectiveness of cellular staining was confirmed through confocal microscopy (see Fig. S2A-G).

Before the application of shear forces, TREK-1 and GM1 lipids displayed a robust correlation (Fig. 2B, C), suggesting a close association between TREK-1 and GM1 lipids. However, after the application of shear forces, this correlation significantly diminished ($p<0.01$ at 50 nm). A similar experiment using a cy3b-labeled anti-TREK-1 antibody yielded nearly identical results, confirming the validity of both our EGFP-dSTORM method and the specificity of the TREK-1 antibody (Fig. S4A) (Fig. S2A).

Following the release of TREK-1 from GM1 lipids, we anticipated that it would undergo a nanoscale repositioning toward PIP_2 clusters. PIP_2 forms distinct nanodomains that are separate from GM1 clusters (Petersen et al., 2016; van den Bogaart et al., 2011; Wang and Richards, 2012) by an average distance of approximately 133 nm in HEK293T cells (Yuan et al., 2022). Cells were subjected to shear forces of 3 dynes/cm^2, permeabilized, fixed, and subsequently

labeled with an anti-PIP_2 antibody. As predicted, the correlation between TREK-1 and PIP_2 was initially low prior to shear application, but it significantly increased after shear forces were applied (Fig. 2D), in contrast to the observations made with GM1 (Fig. 2C). Therefore, shear forces induce TREK-1 to disassociate from GM1 clusters and associate with PIP_2 clusters. Statistical analysis using a Student's t test confirmed the significance of TREK-1 clustering with PIP_2 at both a single radius and multiple point comparisons along the curve.

Subsequently, we investigated the rearrangement of TREK-1 induced by shear forces in the presence of xPLD2. Like mPLD2, we overexpressed xPLD2 in HEK293T cells, mirroring the conditions employed in our electrophysiology experiments in Fig. 1B. Furthermore, as with mPLD2, HEK293T cells were subjected to shear forces, permeabilized, labeled, and imaged with two-color dSTORM.

In the presence of xPLD2, shear caused TREK-1 to leave GM1 domains (Fig. 2E). However, unlike the response observed with mPLD2, the association of TREK-1 with PIP_2 clusters remained relatively weak following shear forces (Fig. 2F), despite an overall increase in TREK-1 and PIP_2 levels in the membrane prior to shear (Fig. S2C-D). Figure 2G shows a model of shear induced movement of TREK-1 from GM1 to PIP_2 clusters.

Mechanism of PLD2 activation by shear.

It is presumed that TREK-1 translocates between nanodomains as a complex with PLD2 (Comoglio et al., 2014). Lacking its own palmitoylation, TREK-1 interacts with PLD2 through its unstructured C-terminus. In earlier research, we demonstrated that cholesterol drives PLD2 associates with GM1 lipids. The application of mechanical force activated PLD2, presumably through the release of PLD2 from GM1 lipids. However, this PLD2 patterning under mechanical shear has not been directly demonstrated with dSTORM.

To validate our proposed mechanism regarding the shear-induced movement of PLD2 with dSTORM, we employed calibrated shear chambers (ibidi μ-Slide $I^{0.4}$ parallel-plate) with cultured C2C12 muscle cells (mouse myocytes) and N2a mouse neuroblastoma cells, which naturally express TREK-1 (see Fig. S2E). Utilizing endogenous expression helped circumvent potential artifacts that may arise from artificially saturating GM1 clusters through protein overexpression.

Our shear experiments were initiated by perfusing phosphate buffered saline (PBS) through the calibrated shear chambers, applying a precisely controlled force of 3 dynes/cm^2. To maintain a constant temperature of 37 ℃, we employed a digitally controlled inline heater. Immediately following the application of shear forces (within <10 seconds), we introduced fixative agents into the shear buffer, facilitating the rapid fixation of cells in their mechanically stimulated state. This approach paralleled the methodology used in our experiments involving rotary shear (see Fig. 3a, S5a), but with tighter control of temperature.

Utilizing two-color dSTORM and analysis by the pair correlation function, we observed that shear forces introduce the mobilization of PLD2 within the cell membrane, and this effect was independent of temperature fluctuations. Prior to the application of shear forces, PLD2 exhibited a strong association with GM1 clusters (Fig. 3B). However, after the application of shear forces, the correlation of PLD2 with GM1 clusters decreased significantly, while it robustly increased in association with PIP_2 clusters (Fig. 3C). Notably, the release of PLD2 from GM1 domains induced by shear forces was more pronounced than the disruption caused by anesthetic agents, as previously reported (Pavel et al., 2020). The stability in temperature, maintained within a range of ± 0.1℃, suggests the mechanism is unlikely to be attributed to the thermal melting of ordered lipids near a phase transition state.

Conducting cluster analysis of GM1 particles subjected to shear revealed a notable reduction in the apparent size of GM1 clusters, decreasing from 167±3 to 131±3 nm

(approximately 20%, Fig. 3d) in C2C12 cells. A similar effect on the size of GM1 clusters was also observed in N2a cells (Fig. 3E). PIP_2 clusters also remained largely intact with a reduction in size (from 154±1 to 139±1) after shear (Fig. S5B).

The observed reduction in cluster size closely resembled the outcomes of prior experiments in which we depleted cholesterol with methyl-beta-cyclodextrin (MBCD) (Pavel et al., 2020; Petersen et al., 2016). Given that MBCD is a known cholesterol removal agent, we conducted assays on N2a cells subjected to orbital fluid shear (3 dynes/cm^2) to examine changes in cholesterol levels. The cells were subjected to 10 min of shear at 37 ℃, followed by fixation.

Our results revealed a 25% reduction in free cholesterol levels in N2a cells exposed to orbital shear ($p<0.001$) (Fig. 3F), which coincided with the activation of PLD (Fig. 3G). Importantly, this decrease in cholesterol was statistically significant $p<0.0001$ and reversible. Allowing the cells to recover for approximately 30 seconds prior to fixation resulted in the restoration of cholesterol levels to those observed in non-sheared cells (Fig. 3F).

In C2C12 cells, TREK-1 and PLD2 exhibited a strong correlation both before (Fig. S5C, grey trace) and after shear (Fig. S5C, red trace), providing further evidence that they form a complex at least intermittently, in both shear and unsheared states. Following shear, a minor fraction of TREK-1 was found to associate with PIP_2 (Fig. S5D). Interestingly, in contrast to HEK293T cells, C2C12 cells displayed minimal TREK-1/GM1 correlation (Fig. S5E, grey trace). Notably, PLD2 regulation is known to be influenced cholesterol(Petersen et al., 2016). In various cell types, we have observed that cultured cells tend to have lower cholesterol levels than human tissues (Wang et al., 2023, 2021; Yuan et al., 2022). These observations lead us to consider the possibility of higher levels of cholesterol in our experimental setup for cultured cells.

Regulation of TREK-1 clustering by cholesterol and GM1 lipids.

Cholesterol levels, especially in the brain, can be notably high (Hansen, 2023; Zhang and Liu, 2015). We hypothesized that cholesterol might influence the endogenous TREK-1 to associate with PLD2 in GM1 clusters. To test this hypothesis, we introduced cholesterol into C2C12 cells using apolipoprotein E (apoE) lipidated with 10% serum, as apoE is a naturally occurring cholesterol transport protein (Wang et al., 2023, 2021; Yuan et al., 2022) (see Fig. 4A). Remarkably, lipidated apoE induced a substantial clustering of TREK-1 with GM1 lipids in membranes of C2C12 cells (Fig. 4B). This effect was also observed with TREK-1 in N2a cells. Intriguingly, the application of fluid shear (3 dynes/cm^2) completely reversed the effect of cholesterol (Fig. 4C).

We anticipated that the cholesterol-induced association of TREK-1 with GM1 lipids would lead to a reduction in TREK-1 currents, as PLD2 would be inhibited due to a lack of substrate. To directly assess the activity of TREK-1 under conditions of elevated cellular cholesterol, we overexpressed TREK-1 in HEK293T cells and quantified the current density in whole cell patch clamp mode, both with and without cholesterol uptake (Fig. 4D). Consistent with our proposed model, TREK-1 current density decreased nearly 2.5-fold in cholesterol-loaded cells, and this reduction in current was statistically significant ($p < 0.05$).

In our earlier investigation, we established that astrocytes play a pivotal role in regulating the clustering of proteins in neurons. This regulation is achieved through the release of apoE-containing particles, which are primarily laden with cholesterol. Remarkably, our studies revealed that cholesterol amplifies the clustering of proteins within GM1 domains. Furthermore, we demonstrated that disrupting the cholesterol synthesis in astrocytes leads to the reversal of protein clustering, as previously reported (Wang et al., 2021). It stands to reason that the same astrocytic cholesterol dynamics could govern the localization of TREK-1 within GM1 lipids in the brain of a mouse.

To investigate the *in vivo* regulation of TREK-1 clustering by astrocytes, we stained 50-micron brain slices obtained from both control mice and mice specifically engineered to lack cholesterol synthesis in astrocytes. The depletion of cholesterol from astrocytes was achieved by targeting sterol regulatory element-binding protein 2 (SREBP2), a crucial regulator of cholesterol synthesis (Ferris et al., 2017; Wang et al., 2021). Before slicing, the brains underwent fixation via whole-body perfusion. The resulting free-floating brain slices were mounted onto circular cover slips using a fiberglass filter paper, which facilitated dSTORM buffer access to the tissue with minimal background interference (see Fig. S4E). These brain slices, taken from coronal sections near the hippocampus were subjected to staining with cy3b-anti-TREK-1 antibody and A647-CTxB. The imaging process encompassed multiple unspecified locations (approximately 10 regions), and subsequent analysis was performed employing the pair correlation function.

In flox control mice (wild type SREBP2), TREK-1/GM1 correlation exhibited a distinct pattern, with TREK-1 clustering near GM1 (Fig. 4E), aligning with the GM1 correlation seen in N2a cells with elevated levels of cholesterol (Fig. 4B). As anticipated, in the brains of mice with astrocyte-specific SREBP2 deficiency, TREK-1 displayed a reduced association with GM1 lipids ($p<0.0001$). These findings serve as compelling evidence that, in the brain of an animal, astrocytic cholesterol serves as a critical regulator of TREK-1's affinity for inhibitory GM1 clusters.

Figure 4F presents a comprehensive model detailing the regulation of TREK-1 by astrocyte-derived cholesterol, using the insights derived from both cultured cells and *ex vivo* studies. In this model, cholesterol originating from astrocytes is transported to neurons via apoE. Under conditions of elevated membrane cholesterol, TREK-1 forms associations with inhibitory GM1 lipids, a scenario in which PLD2 has limited substrate availability. Conversely, when membrane cholesterol levels are reduced, TREK-1 relocates away from GM1 lipids toward activating PIP_2 lipids. In this context, PLD2 gains improved access to its substrate phosphatidylcholine (PC),

leading to the production of lipid agonists such as PA, which ultimately evoke activation of the TREK-1 channel.

Direct activation of PLD2 by osmotic stretch.

Osmotic stretch is a well-documented activator of TREK-1 (Patel et al., 1998). To investigate whether osmotic stretch also activates PLD2, we conducted experiments to monitor PLD product release in live cells subjected to hypotonic stretch. Our findings revealed that membrane stretch by a 70 mOsm swell (representing a high degree of stress) led to approximately 50% increase in PLD2 activity in N2a cells (Fig. 5A). It is worth noting that this level of activation, although significant, was less pronounced compared to shear stress in N2a cells (Fig. 3E), which increased approximately 3-fold in activity.

Subsequently, we conducted dSTORM experiments to investigate whether stretch had the capacity to release PLD2 from GM1 lipids within the membranes of N2a cells. In these experiments, cells were exposed to either a hypotonic solution with an osmolality of 70 mOsm (indicating a state of swelling) or an isotonic solution with an osmolality of 310 mOsm (representing a control condition) for 15 min at 37 ℃. Following this treatment, the cells were fixed, labeled, and subjected to imaging using the same procedures employed in the shear stress experiments. Our results, consistent with the outcomes of shear stress experiments and PLD2 assay, clearly demonstrated a discernible shift in the spatial distribution of PLD2, transitioning from ordered GM1 clusters to the PIP_2 clusters after osmotic stretch (Fig. 5B-D).

PA regulation of mechanosensitivity thresholds *in vivo*

In order to gain deeper insights into the *in vivo* role of PLD2 in mechanotransduction, we conducted investigations into mechano-thresholds and pain perception in Drosophila, employing a PLD-knockout model (Thakur et al., 2016). It is worth noting that, while the specific downstream effectors of PLD in fruit flies remain unidentified, and they possess only distantly related TREK-1

orthologs, (as discussed in a later section), the utilization of fruit flies as a model organism is advantageous because they possess a single PLD gene (*dPLD)*.

Our analysis revealed the presence of GM1 domains in dissected fly brains, and we observed that dPLD exhibited a robust response to shear stress of 3 dynes/cm^2 when cultured in neuronally derived fly cell line, BG2-c2 (see Fig. 6A-B). The activity of PLD increased by nearly fourfold in the fly cell line (Fig. 6A), a result consistent with the response of PLD to mechanical force observed in HEK293T cells (Fig. 3G).

Subsequently, we preceded to examine the *in vivo* role for PA in mechanosensation employing single-animal measurements of arousal threshold (Murphy et al., 2017, 2016) (see Fig. S6A). The arousal assay quantifies the amount of mechanical stimulation required to elicit movement from a resting fly. Over a period of 24 hours, the flies were exposed to a series of incremental vibrational stimuli every 30 minutes. For each series, the threshold of stimulation necessary to induce movement in the fly, as indicated by observable motion, was recorded using automated machine vision tracking. These recorded measurements were then compared to genetically matched control groups.

PLD^{null} flies exhibited a notably lower arousal threshold compared to their control counterparts (Fig. 6C). This lower arousal implies an increased sensitivity to mechanical force. Furthermore, we employed a neuronal-specific driver, Nsyb GAL4, in conjunction with a PLD RNAi line (PLD-KD) to investigate the role of PLD in the central nervous system. The neuronal knockdown of PLD yielded a similar increase in mechanosensitivity, providing clear evidence that this phenotype is specific to neuronal functions (Fig. 6D).

Furthermore, we conducted assessments to determine the role of PLD in fly shock avoidance, serving as a measure of an adverse electrical stimulus. To assess their responses, PLD-KD flies were positioned at the choice-point of a T maze, where they were given the option

to select between a chamber inducing a noxious shock or a non-shock control chamber (Drago and Davis, 2016). Flies were subjected to incrementally increasing voltages of electrical shock. Our findings revealed that PLD^{null} flies exhibited heightened sensitivity to electric shock compared to control groups (Fig. 6E-F). In Fig. 6G, we present a potential model illustrating how PA may contribute to mechanosensitivity in a fly.

Discussion

In summary, our findings collectively demonstrate that the spatial distribution of TREK-1 and PLD2 in association with GM1 and PIP_2 lipids, along with the generation of PLD2-derived PA, are essential for eliciting the complete mechanically evoked current from TREK-1 in a biological membrane. Furthermore, the disruption of PLD2 localization within a lipid nanodomain provides a compelling explanation for how the C-terminus confers mechanosensitivity to a channel, particularly when the domain lacks structural integrity.

In contrast, the activation of purified TREK-1 in soy PC does not necessitate the involvement of the C-terminus, as indicated by prior research (Stephen G Brohawn et al., 2014). This observation implies the existence of a PLD2-independent mechanism of action. The precise relative contributions of the two mechanisms in endogenous tissue remain unclear. Notably, in HEK293T cells, a current density of 0.05 pA/cm^2 current density (representing less than 10% of the total stretch current) was found to be PLD2 independent (see Fig. 1C inset). This observation raises the possibility that the localization of TREK-1 to mechanosensitive lipids essential for its activation might be lacking in this context, or alternatively, the propagation of tension within the plasma membrane might differ. Consequently, there is a need for a more comprehensive understanding of TREK-1 spatial patterning within specific cell types, coupled with an understanding of stretch induced tension in the different lipid nanodomains. Furthermore, it is

plausible that a portion of the PLD2-dependent stretch current merely augments the direct mechanosensitivity of TREK-1. However, it is important to note that this enhancement mechanism is not obligatory, as the channel is directly activated by PA in purified lipids absent stretch and tension (Cabanos et al., 2017). This can also explain the discrepancies between liposome-based Mechanosensitivity since crude soy extracts (azolectin) are known to contain anionic lipids, thus may negate the need for a C-terminus and providing the PA needed for full TREK activation.

As mentioned previously, PLD2 is a soluble enzyme that associates with the membrane through palmitate. Given its lack of a transmembrane domain, mechanisms of mechanosensation involving hydrophobic mismatch, tension, midplane bending, and curvature can be largely ruled out, leaving the kinetic mechanism as the most plausible. The palmate moiety establishes van der Waals bonds with the GM1 lipids. The disruption of these bonds is necessary for PLD to disassociate from GM1 lipids, suggesting a mechanism akin to 'shear thinning' within GM1 clusters. Shear thinning is a term in rheology that describes the phenomenon wherein viscous mixtures become less viscous in response to shear or stretching forces (Küçüksönmez and Servantie, 2020). This process is inherently kinetic in nature and operates by mechanically disrupting noncovalent bonds, thereby allowing the molecules to move relative to one another (See Fig. 3H and S5F for detailed description).

The spatial patterning of TREK-1 with PIP_2 clusters may depend on the channel's conformational state, as evidenced by the observation that xPLD/TREK-1 combination exhibited reduced associated with PIP_2 after shear compared to the mPLD/TREK-1 combination (Fig. 2D,F) despite an increase in the levels of PIP_2 and TREK-1 expression prior to shear (Fig. S2C-D,G). This observation aligns with the up down model of the gating helix (Stephen G. Brohawn et al., 2014). As illustrated in Fig. 5D, we propose a theoretical mechanism that accounts for the coordinated signaling involving PA and for combined PA signaling and direct force from lipid in a biological membrane. This mechanism suggests that conformational changes conducive to the

helix-up (open) position is sustained only when PLD2 is present and capable of producing localized PA. In the absence of PA, PIP_2 forces the channel closed (Cabanos et al., 2017; Chemin et al., 2007b) and the helix in the down position (Fig. S3E-F).

In control experiments that estimated protein levels through fluorescent labeling, we observed a significant decrease in TREK-1 protein levels after fixation with mPLD2 or shear for 15 min (Fig. S2G). While it is conceivable that this decline in protein levels might have occurred in less than 2 milliseconds, i.e., faster than we are able to observe (see Fig. S3D), which could explain the loss of TREK-1 current in Fig. 1b, independent of local PA gating of TREK-1, endocytosis, the process that removes TREK-1 from the plasma membrane, is not likely to occur in less than 2 ms (Soykan et al., 2017). Furthermore, the reduction in TREK-1 levels was comparable when wt. PLD2 was employed (Fig. S2G), suggesting that alterations in protein levels are unlikely to account for the diminished TREK-1 pressure currents observed with xPLD2 in Fig. 1B.

It is important to note that PLD2 is recognized for its ability to enhance endocytosis (Du et al., 2004). Specifically, xPLD2 has been shown to inhibit both agonist induced and constitutive endocytosis of μ-opioid receptor, effectively retaining the receptor on the membrane (Koch et al., 2006). The phenomenon of membrane retention is not unique to the μ-opioid receptor but extends to many proteins including Rho (Wheeler et al., 2015), ARF (Rankovic et al., 2009), and ACE2 (Du et al., 2004) among others. Consequently, it is not surprising that the overexpression of xPLD resulted in an increase in TREK-1 surface expression (Fig. S2C,G). Conversely, the overexpression of mPLD led to the lowest levels of TREK_1 expression, which aligns with its propensity for promoting endocytosis (Fig. S2G,H). Given that mPLD2 yielded the highest mechanically evoked TREK-1 current despite the lowest protein levels, it appears unlikely that protein expression levels are the limiting factor governing mechanically evoked TREK-1 currents in HEK293T cells.

The latency of PLD2 dependent activation is important as it offers insights into the potential physiological processes in which PLD2 may play a role in mechanotransduction. Drawing from estimates involving diffusion from GM1 to PIP_2, we estimated a latency of ~650 μs (Petersen et al., 2016). To establish an upper temporal limit for PLD2 to become activated and generate PA in proximity to TREK-1, we leveraged the rate of increase in TREK-1 activity observed with WT PLD2. We observed initial TREK-1 currents almost immediately and these currents became notably significant within 2.1 ms at a pressure of 60 mmHg (Fig. S3D). This timeframe is highly likely to be faster than the margin of error associated with our instrument setup. While we did not perform a precise calibration of our setup's error, conservative estimates based on manufacturer specifications suggest an upper limit of approximately 10 milliseconds.

The requirement for both PLD2 activity and the C-terminus to activate TREK-1 by pressure provides further validation for the previously proposed conclusion that TREK-1 is gated by a local high concentration of PA (Cabanos et al., 2017; Comoglio et al., 2014). In theory, PLD2 activity could elevate global PA levels to a point where TREK-1 becomes activated without the need for spatial patterning through protein-protein interactions. However, our experiments with truncated TREK-1 and 60 mmHg pressure in HEK293T cells did not support this hypothesis (Fig. 1C).

Our findings regarding the mechanism we identified remained consistent across cell types (HEK, N2a, C2C12, mouse neurons) despite their significant differences in cellular characteristics. We were able to induce protein-lipid domain associations in all these cell types through the manipulation of cholesterol levels. This intriguing observation suggests a potential avenue of research to investigate whether cholesterol or other lipids undergo significant changes at sites where mechanosensation is known to occur, such as at the termini of low- or high-threshold mechanoreceptors (Handler and Ginty, 2021). It's conceivable that various neuronal types and the channels localized within them adapt to different types of mechanosensation by modulating the lipid environment where sensory perception is most critical. For instance, inflammation-

induced cholesterol uptake (Hansen and Wang, 2023) might sensitize channels to pain perception (Petersen et al., 2020).

Additionally, our experiments with flies highlight the importance of the upstream effectors in these systems. While the specific binding partners for PLD2 and its potential downstream effects in flies remain unknown, the observed phenotypes strongly suggest that PLD plays a crucial role in normal sensory perception which appears to be more evolutionarily conserved than TREK-1. It is possible that a single lipid or a mechanism regulating multiple channels simultaneously may have a more significant impact compared to the modulation of a single channel.

The regulation of mechanosensation and electric shock responses in Drosophila by PA (Fig. 6) provides *in vivo* support for the growing understanding of the role of anionic lipids in setting force-sensing thresholds. For example, PIP_2 sets the threshold for mechanical B-cell activation (Wan et al., 2018), while sphingosine-1-phosphate (S1P), a lipid similar to PA, regulates pain in mice (Hill et al., 2018). The activation of PLD2 by mechanical force and substrate presentation helps elucidate how an enzyme could directly set pain thresholds and mechanosensitivity via canonical mechanosensitive ion channels and endocytosis.

Palmitoylation, a modification found in many important signaling molecules including tyrosine kinases, GTPases, CD4/8, and almost all G-protein alpha subunits (Aicart-Ramos et al., 2011), can target proteins to GM1 domains (Levental et al., 2010). The spatial patterning of these palmitoylated proteins or their binding partner, by mechanical force may alter the availability of substrates and affect downstream signaling. Spatial patterning along with its effect on palmitoylated G-proteins likely contributes to the mechanosensitivity observed in many GPCRs (Gudi et al., 1998; Storch et al., 2012; Wei et al., 2018; Xu et al., 2018). Many ion channels are also palmitoylated (Shipston, 2011). For example, the voltage-gated sodium channel (Na_v)1.9 clusters with GM1 lipids, and disrupting this clustering (e.g., by chemically removing cholesterol)

induces a corresponding pain response (Amsalem et al., 2018; Wan et al., 2018). Similarly, sphingosine-1-phosphate (S1P), an anionic lipid similar to PA, regulates pain in mice (Hill et al., 2018).

Lastly, it's worth noting that PIP2 gates many ion channels (Cabanos et al., 2017; Chung et al., 2019; Hansen, 2015; Hansen et al., 2011; Robinson et al., 2019), and the spatial patterning induced by PIP2 should be considered in combination with the direct effect of the lipid on the channel. Cholesterol, known to bind directly to and modulate channels (Levitan et al., 2014), should also be considered separately from its influence on spatial patterning through GM1 lipids. These direct lipid effects are likely to interact with spatial patterning to collectively regulate the biochemical processes within a cell.

Acknowledgements

We thank Tamara Boto and Seth Tomchik for their assistance in the Drosophila shock experiments, Michael Frohman from Stony Brook for the mouse PLD and mutant PLD cDNA, Steven Long from Memorial Sloan Kettering for human TREK-1-GFP, Padinjat Raghu for the PLD mutant Drosophila, Andrew S. Hansen for PLD experiments, multiple aspects of experimental design and discussion, Yul Young Park for the electrophysiology experimentation, and Carl Ebeling for his help and discussion on the imaging analysis. This work was supported by a Director's New Innovator Award to S.B.H. (DP2NS087943) and R01 (R01NS112534) from the National Institutes of Health, an R01 to W.W.J. (R01AG045036) from the National Institute on Aging, and a graduate fellowship from the Joseph B. Scheller & Rita P. Scheller Charitable Foundation to E.N.P. We are grateful to the JPB Foundation for the purchase of a super resolution microscope. The authors declare no conflict of interest.

Author Contributions

Conceptualization, E.N.P. and S.B.H.; Methodology, E.N.P., M.G., K.R.M, and S.B.H; Investigation, E.N.P., M.G., and K.R.M; Resources, W.W.J., E.M.J., and S.B.H.; Writing – Original Draft, E.N.P. and S.B.H.; Writing – Review and Editing, E.N.P., M.G., M.A.P, E.M.J., and S.B.H.; Supervision, W.W.J. and S.B.H.; Funding Acquisition, W.W.J. and S.B.H.

Works Cited

Aicart-Ramos C, Valero RA, Rodriguez-Crespo I. 2011. Protein palmitoylation and subcellular trafficking. *Biochim Biophys Acta - Biomembr* **1808**:2981–2994. doi:10.1016/j.bbamem.2011.07.009

Amsalem M, Poilbout C, Ferracci G, Delmas P, Padilla F. 2018. Membrane cholesterol depletion as a trigger of Nav1.9 channel-mediated inflammatory pain. *EMBO J* **37**:1–19. doi:10.15252/embj.201797349

Berrier C, Pozza A, De Lacroix De Lavalette A, Chardonnet S, Mesneau A, Jaxel C, Maire M Le, Ghazi A, le Maire M, Ghazi A. 2013. The purified mechanosensitive channel TREK-1 is directly sensitive to membrane tension. *J Biol Chem* **288**:27307–14. doi:10.1074/jbc.M113.478321

Brohawn SG. 2015. How ion channels sense mechanical force: insights from mechanosensitive K2P channels TRAAK, TREK1, and TREK2. *Ann N Y Acad Sci* **1352**:20–32. doi:10.1111/nyas.12874

Brohawn Stephen G., Campbell EB, MacKinnon R. 2014. Physical mechanism for gating and mechanosensitivity of the human TRAAK K+ channel. *Nature* **516**:126–130. doi:10.1038/nature14013

Brohawn Stephen G, Su Z, Mackinnon R. 2014. Mechanosensitivity is mediated directly by the lipid membrane in TRAAK and TREK1 K+ channels. *Proc Natl Acad Sci U S A* **111**:3614–9. doi:10.1073/pnas.1320768111

Cabanos C, Wang M, Han X, Hansen SB. 2017. A Soluble Fluorescent Binding Assay Reveals PIP2 Antagonism of TREK-1 Channels. *Cell Rep* **20**:1287–1294. doi:10.1016/j.celrep.2017.07.034

Call IM, Bois JL, Hansen SB. 2023. Super-resolution imaging of potassium channels with genetically encoded EGFP. *BioRxiv*. doi:10.1101/2023.10.13.561998

Chemin J, Patel AJ, Delmas P, Sachs F, Lazdunski M, Honore E. 2007a. Regulation of the Mechano-Gated K 2P Channel TREK-1 by Membrane Phospholipids. doi:10.1016/S1063-5823(06)59007-6

Chemin J, Patel AJ, Duprat F, Sachs F, Lazdunski M, Honore E. 2007b. Up- and down-regulation of the mechano-gated K2P channel TREK-1 by PIP2 and other membrane phospholipids. *Pflugers Arch Eur J Physiol* **455**:97–103. doi:10.1007/s00424-007-0250-2

Chung H-WW, Petersen EN, Cabanos C, Murphy KR, Pavel MA, Hansen AS, Ja WW, Hansen SB. 2019. A Molecular Target for an Alcohol Chain-Length Cutoff. *J Mol Biol* **431**:196–209. doi:10.1016/j.jmb.2018.11.028

Coltharp C, Yang X, Xiao J. 2014. Quantitative analysis of single-molecule superresolution images. *Curr Opin Struct Biol* **28**:112–121. doi:10.1016/j.sbi.2014.08.008

Comoglio Y, Levitz J, Kienzler M a., Lesage F, Isacoff EY, Sandoz G. 2014. Phospholipase D2 specifically regulates TREK potassium channels via direct interaction and local production of phosphatidic acid. *Proc Natl Acad Sci U S A* **111**:13547–52. doi:10.1073/pnas.1407160111

Cox CD, Bavi N, Martinac B. 2019. Biophysical Principles of Ion-Channel-Mediated Mechanosensory Transduction. *Cell Rep*. doi:10.1016/j.celrep.2019.08.075

Drago I, Davis RL. 2016. Inhibiting the Mitochondrial Calcium Uniporter during Development Impairs Memory in Adult Drosophila. *Cell Rep* **16**:2763–2776. doi:10.1016/j.celrep.2016.08.017

Du G, Huang P, Liang BT, Frohman MA. 2004. Phospholipase D2 localizes to the plasma

membrane and regulates angiotensin II receptor endocytosis. *Mol Biol Cell* **15**:1024–1030. doi:10.1091/mbc.E03-09-0673

Ferris HA, Perry RJ, Moreira G V, Shulman GI, Horton JD, Kahn CR. 2017. Loss of astrocyte cholesterol synthesis disrupts neuronal function and alters whole-body metabolism. *Proc Natl Acad Sci U S A* **114**:1189–1194. doi:10.1073/pnas.1620506114

Gudi S, Nolan JP, Frangos JA. 1998. Modulation of GTPase activity of G proteins by fluid shear stress and phospholipid composition. *Proc Natl Acad Sci U S A* **95**:2515–2519. doi:10.1073/pnas.95.5.2515

Hahn C, Schwartz MA. 2009. Mechanotransduction in vascular physiology and atherogenesis. *Nat Rev Mol Cell Biol* **10**:53–62. doi:10.1038/nrm2596

Handler A, Ginty DD. 2021. The mechanosensory neurons of touch and their mechanisms of activation. *Nat Rev Neurosci* **22**:521–537. doi:10.1038/s41583-021-00489-x

Hansen SB. 2023. Cholesterol's Function and Origin in the Alzheimer's Disease Brain. *J Alzheimer's Dis* **94**:1–2. doi:10.3233/jad-230538

Hansen SB. 2015. Lipid agonism: The PIP2 paradigm of ligand-gated ion channels. *Biochim Biophys Acta* **1851**:620–628. doi:10.1016/j.bbalip.2015.01.011

Hansen SB, Tao X, MacKinnon R. 2011. Structural basis of PIP2 activation of the classical inward rectifier K+ channel Kir2.2. *Nature* **477**:495–8. doi:10.1038/nature10370

Hansen SB, Wang H. 2023. The shared role of cholesterol in neuronal and peripheral inflammation. *Pharmacol Ther* **249**:108486. doi:10.1016/j.pharmthera.2023.108486

Hill RZ, Hoffman BU, Morita T, Campos SM, Lumpkin EA, Brem RB, Bautista DM. 2018. The signaling lipid sphingosine 1-phosphate regulates mechanical pain. *Elife* **7**:e33285. doi:10.7554/eLife.33285

1 Honoré E. 2007. The neuronal background K2P channels: focus on TREK1. *Nat Rev Neurosci*
2 **8**:251–261. doi:10.1038/nrn2117

3 Julius D. 2001. Molecular mechanisms of nociception . *Nature* **413**:203–210.
4 doi:10.1038/35093019

5 Koch T, Wu DF, Yang LQ, Brandenburg LO, Höllt V. 2006. Role of phospholipase D2 in the
6 agonist-induced and constitutive endocytosis of G-protein coupled receptors. *J Neurochem*
7 **97**:365–372. doi:10.1111/j.1471-4159.2006.03736.x

8 Küçüksönmez E, Servantie J. 2020. Shear thinning and thickening in dispersions of spherical
9 nanoparticles. *Phys Rev E* **102**:1–9. doi:10.1103/PhysRevE.102.012604

10 Kwon DH, Zhang F, McCray BA, Feng S, Kumar M, Sullivan JM, Im W, Sumner CJ, Lee SY.
11 2023. TRPV4-Rho GTPase complex structures reveal mechanisms of gating and disease.
12 *Nat Commun* **14**:1–15. doi:10.1038/s41467-023-39345-0

13 Lang T, Bruns D, Wenzel D, Riedel D, Holroyd P, Thiele C, Jahn R. 2001. SNAREs are
14 concentrated in cholesterol-dependent clusters that define docking and fusion sites for
15 exocytosis. *EMBO J*. doi:10.1093/emboj/20.9.2202

16 Levental I, Lingwood D, Grzybek M, Coskun U, Simons K. 2010. Palmitoylation regulates raft
17 affinity for the majority of integral raft proteins. *Proc Natl Acad Sci* **107**:22050–22054.
18 doi:10.1073/pnas.1016184107

19 Levitan I, Singh DK, Rosenhouse-Dantsker A. 2014. Cholesterol binding to ion channels. *Front*
20 *Physiol* **5 FEB**:1–14. doi:10.3389/fphys.2014.00065

21 Lin HH, Ng KF, Chen TC, Tseng WY. 2022. Ligands and Beyond: Mechanosensitive Adhesion
22 GPCRs. *Pharmaceuticals* **15**:1–18. doi:10.3390/ph15020219

23 McDermott M, Wakelam MJO, Morris AJ. 2004. Phospholipase D. *Biochem Cell Biol* **82**:225–53.

doi:10.1139/o03-079

Moon S, Yan R, Kenny SJ, Shyu Y, Xiang L, Li W, Xu K. 2017. Spectrally Resolved, Functional Super-Resolution Microscopy Reveals Nanoscale Compositional Heterogeneity in Live-Cell Membranes. *J Am Chem Soc* **139**:10944–10947. doi:10.1021/jacs.7b03846

Murphy KR, Deshpande SA, Yurgel ME, Quinn JP, Weissbach JL, Keene AC, Dawson-Scully K, Huber R, Tomchik SM, Ja WW. 2016. Postprandial sleep mechanics in Drosophila. *Elife* **5**:1–19. doi:10.7554/eLife.19334

Murphy KR, Park JH, Huber R, Ja WW. 2017. Simultaneous measurement of sleep and feeding in individual Drosophila. *Nat Protoc* **12**:2355–2366. doi:10.1038/nprot.2017.096

Patel AJ, Honoré E, Maingret F, Lesage F, Fink M, Duprat F, Lazdunski M. 1998. A mammalian two pore domain mechano-gated S-like K+ channel. *EMBO J* **17**:4283–90. doi:10.1093/emboj/17.15.4283

Pavel MA, Petersen EN, Wang H, Lerner RA, Hansen SB. 2020. Studies on the mechanism of general anesthesia. *Proc Natl Acad Sci U S A* **117**:13757–13766. doi:10.1073/pnas.2004259117

Petersen EN, Chung H-W, Nayebosadri A, Hansen SB. 2016. Kinetic disruption of lipid rafts is a mechanosensor for phospholipase D. *Nat Commun* **7**:13873. doi:10.1038/ncomms13873

Petersen EN, Pavel MA, Wang H, Hansen SB. 2020. Disruption of palmitate-mediated localization; a shared pathway of force and anesthetic activation of TREK-1 channels. *Biochim Biophys Acta - Biomembr* **1862**:183091. doi:10.1016/j.bbamem.2019.183091

Raghunathan K, Kenworthy AK. 2018. Dynamic pattern generation in cell membranes: Current insights into membrane organization. *Biochim Biophys acta Biomembr* **1860**:2018–2031. doi:10.1016/j.bbamem.2018.05.002

Ranade SS, Syeda R, Patapoutian A. 2015. Mechanically Activated Ion Channels. *Neuron* **87**:1162–79. doi:10.1016/j.neuron.2015.08.032

Rankovic M, Jacob L, Rankovic V, Brandenburg L-OO, Schröder H, Höllt V, Koch T. 2009. ADP-ribosylation factor 6 regulates mu-opioid receptor trafficking and signaling via activation of phospholipase D2. *Cell Signal* **21**:1784–1793. doi:10.1016/j.cellsig.2009.07.014

Robinson C V., Rohacs T, Hansen SB. 2019. Tools for Understanding Nanoscale Lipid Regulation of Ion Channels. *Trends Biochem Sci* **44**:795–806. doi:10.1016/j.tibs.2019.04.001

Schneck DJ. 1992. Mechanics of Muscle, Dynamic Behaviour of Materials Vol 1. New York: New York University Press. doi:10.1007/978-3-319-00771-7-1

Shipston MJ. 2011. Ion channel regulation by protein palmitoylation. *J Biol Chem* **286**:8709–8716. doi:10.1074/jbc.R110.210005

Soykan T, Kaempf N, Sakaba T, Vollweiter D, Goerdeler F, Puchkov D, Kononenko NL, Haucke V. 2017. Synaptic Vesicle Endocytosis Occurs on Multiple Timescales and Is Mediated by Formin-Dependent Actin Assembly. *Neuron* **93**:854-866.e4. doi:10.1016/j.neuron.2017.02.011

Storch U, Mederos y Schnitzler M, Gudermann T. 2012. G protein-mediated stretch reception. *Am J Physiol - Hear Circ Physiol* **302**:H1241-9. doi:10.1152/ajpheart.00818.2011

Tanaka KAK, Suzuki KGN, Shirai YM, Shibutani ST, Miyahara MSH, Tsuboi H, Yahara M, Yoshimura A, Mayor S, Fujiwara TK, Kusumi A. 2010. Membrane molecules mobile even after chemical fixation. *Nat Methods* **7**:865–866. doi:10.1038/nmeth.f.314

Teng J, Loukin S, Anishkin A, Kung C. 2015. The force-from-lipid (FFL) principle of mechanosensitivity, at large and in elements. *Pflügers Arch Eur J Physiol* **467**:27–37. doi:10.1007/s00424-014-1530-2

1 Thakur R, Panda A, Coessens E, Raj N, Yadav S, Balakrishnan S, Zhang Q, Georgiev P, Basak
2 B, Pasricha R, Wakelam MJO, Ktistakis NT, Raghu P. 2016. Phospholipase D activity
3 couples plasma membrane endocytosis with retromer dependent recycling. *Elife* **5**:1–23.
4 doi:10.7554/eLife.18515

5 Toschi A, Lee E, Xu L, Garcia A, Gadir N, Foster DA. 2009. Regulation of mTORC1 and mTORC2
6 complex assembly by phosphatidic acid: competition with rapamycin. *Mol Cell Biol* **29**:1411–
7 20. doi:10.1128/MCB.00782-08

8 van den Bogaart G, Meyenberg K, Risselada HJ, Amin H, Willig KI, Hubrich BE, Dier M, Hell SW,
9 Grubmüller H, Diederichsen U, Jahn R. 2011. Membrane protein sequestering by ionic
10 protein-lipid interactions. *Nature* **479**:552–5. doi:10.1038/nature10545

11 Veatch SL, Machta BB, Shelby SA, Chiang EN, Holowka DA, Baird BA. 2012. Correlation
12 functions quantify super-resolution images and estimate apparent clustering due to over-
13 counting. *PLoS One* **7**. doi:10.1371/journal.pone.0031457

14 Wan Z, Xu C, Chen X, Xie H, Li Z, Wang J, Ji X, Chen H, Ji Q, Shaheen S, Xu Y, Wang F, Tang
15 Z, Zheng J-S, Chen W, Lou J, Liu W. 2018. PI(4,5)P2 determines the threshold of mechanical
16 force-induced B cell activation. *J Cell Biol* jcb.201711055. doi:10.1083/jcb.201711055

17 Wang H, Feng Z, Del Signore SJ, Rodal AA, Xu B. 2018. Active Probes for Imaging Membrane
18 Dynamics of Live Cells with High Spatial and Temporal Resolution over Extended Time
19 Scales and Areas. *J Am Chem Soc* **140**:3505–3509. doi:10.1021/jacs.7b13307

20 Wang H, Kulas JA, Wang C, Holtzman DM, Ferris HA, Hansen SB. 2021. Regulation of beta-
21 amyloid production in neurons by astrocyte-derived cholesterol. *Proc Natl Acad Sci U S A*
22 **118**:e2102191118. doi:10.1073/pnas.2102191118

23 Wang H, Yuan Z, Pavel MA, Jablonski SM, Jablonski J, Hobson R, Valente S, Reddy CB, Hansen

SB. 2023. The role of high cholesterol in SARS-CoV-2 infectivity. *J Biol Chem* **299**:104763. doi:10.1016/j.jbc.2023.104763

Wang J, Richards D a. 2012. Segregation of PIP2 and PIP3 into distinct nanoscale regions within the plasma membrane. *Biol Open* **1**:857–62. doi:10.1242/bio.20122071

Wei WC, Bianchi F, Wang YK, Tang MJ, Ye H, Glitsch MD. 2018. Coincidence Detection of Membrane Stretch and Extracellular pH by the Proton-Sensing Receptor OGR1 (GPR68). *Curr Biol* **28**:3815-3823.e4. doi:10.1016/j.cub.2018.10.046

Wheeler DS, Underhill SM, Stolz DB, Murdoch GH, Thiels E, Romero G, Amara SG. 2015. Amphetamine activates Rho GTPase signaling to mediate dopamine transporter internalization and acute behavioral effects of amphetamine. *Proc Natl Acad Sci U S A* **112**:E7138–E7147. doi:10.1073/pnas.1511670112

Wilde C, Mitgau J, Suchý T, Schöneberg T, Liebscher I. 2022. Translating the force—mechano-sensing GPCRs. *Am J Physiol - Cell Physiol* **322**:C1047–C1060. doi:10.1152/ajpcell.00465.2021

Xu J, Mathur J, Vessières E, Hammack S, Nonomura K, Favre J, Grimaud L, Petrus M, Francisco A, Li J, Lee V, Xiang F, Mainquist JK, Cahalan SM, Orth AP, Walker JR, Ma S, Lukacs V, Bordone L, Bandell M, Laffitte B, Xu Y, Chien S, Henrion D, Patapoutian A. 2018. GPR68 Senses Flow and Is Essential for Vascular Physiology. *Cell* **173**:762-775.e16. doi:10.1016/j.cell.2018.03.076

Yuan Z, Hansen SB. 2023. Cholesterol Regulation of Membrane Proteins Revealed by Two-Color Super-Resolution Imaging. *Membranes (Basel)* **13**:250. doi:10.3390/membranes13020250

Yuan Z, Pavel MA, Wang H, Kwachukwu JC, Mediouni S, Jablonski JA, Nettles KW, Reddy CB, Valente ST, Hansen SB. 2022. Hydroxychloroquine blocks SARS-CoV-2 entry into the

endocytic pathway in mammalian cell culture. *Commun Biol* **5**:958. doi:10.1038/s42003-022-03841-8

Zhang J, Liu Q. 2015. Cholesterol metabolism and homeostasis in the brain. *Protein Cell* **6**:254–264. doi:10.1007/s13238-014-0131-3

1 Materials and Methods

2 **Cell Culture and Gene Expression**

3 HEK293T cells (ATCC Cat# CRL-3216, RRID:CVCL_0063) were cultured in DMEM (Corning
4 cellgro) with 10% FBS, 100 units/mL penicillin, and 100 μg/mL streptomycin. Cells were plated
5 on poly-D-lysine-coated 12 mm microscope cover glass at approximately 12h, 36h, or 60 hours
6 before transfection with genes for target proteins. Transfections were performed using X-
7 tremeGENE 9 DNA transfection agent (Roche Diagnostics). Full-length human TREK-1(TREK-1
8 FL) with C-terminus GFP tag in pCEH vector was obtained from Dr. Stephen Long. Mouse PLD2
9 constructs (mPLD2) and inactive mutant (K758R single mutation, xPLD2) without GFP tag in
10 pCGN vector were provided by Dr. Michael Frohman. TREK-1 constructs were co-transfected
11 with mPLD2 or xPLD2 at a 1:4 ratio (0.5g of TREK-1 and 2g of PLD DNA)(Comoglio et al., 2014).
12 All the salts for internal/external solutions were purchased from either Sigma or Fisher Scientific.

13 **Electrophysiology**

14 The transfected HEK293T cells were used in 24~36 hours after transfection for standard excised
15 inside-out patch-clamp recordings of TREK-1(Stephen G Brohawn et al., 2014; Comoglio et al.,
16 2014). Currents were recorded at room temperature using an Axopatch 200B amplifier and
17 Digidata 1440A (Molecular Devices). Borosilicate glass electrode pipettes (B150-86-10, Sutter
18 Instrument) were pulled with the Flaming/Brown micropipette puller (Model P-1000, Sutter
19 instrument) resulting in 3~6 MΩ resistances with the pipette solution (in mM): 140 NaCl, 5 KCl, 1
20 CaCl2, 3 MgCl2, 10 TEA-Cl, 10 HEPES, pH 7.4 (adjusted with NaOH). Bath solution consists of
21 (in mM): 140 KCl, 3 MgCl2, 5 EGTA, 10 TEA-Cl, 10 HEPES, pH 7.2 (adjusted with KOH). Low
22 concentration of TEA (10 mM), was added into both pipette/bath solutions to block the
23 endogenous potassium channels in HEK293T cells. Patch electrodes were wrapped with parafilm

to reduce capacitance. Currents measured using Clampex 10.3(Molecular Devices) were filtered at 1 kHz, sampled at 20 kHz, and stored on a hard disk for later analysis.

Pressure clamping on the patch was performed using high speed pressure clamping system (ALA Scientific) through the Clampex control. Data was analyzed off-line by a homemade procedure using IgorPro 6.34A (WaveMetrics).

TREK-1 current, either co-expressed with mPLD2 or xPLD2 was activated by negative pressure steps from 60 to 0 mmHg in 10 mmHg decrements at +30 mV membrane potential, and 5 traces for each case were recorded and averaged for the analysis. Patch size was estimated using the current density (I_density; pA/μm^2). Then, a Boltzman equation, I_density = base +{max/[1+exp((P50-P)/slope)]} was used to fit the data with a constraint of base=1 due to poor saturation of the current at high pressure. P is the applied pressure, P50 is the pressure that activates 50% of maximum current measured (non-saturating), and slope shows the sensitivity of current activation by pressure. In some experiments with hTREK-1+xPLD2 co-expression where the activated currents were too small to fit to the Boltzman equation, the current amplitude at P=-30 mmHg (I_m30) was compared with its 5x standard deviation(I_5xSD). If I_m30 < I_5xSD, the experiment was excluded from the Boltzman equation fitting and corresponding P50-slope analysis. This empirical rule (we call it 5xSD rule) can discern 4 out of 5 wild type (TREK-1 FL) cell-attached recording cases as null experiments suggesting that it could be a usable/useful empirical criterion for our experiment. Then, the current density at -60 mmHg and P50-slope data were used for statistical analysis. Mann Whitney test was done to assess statistical significance using Prism6 (GraphPad software), and outliers were eliminated using a built-in function in Prism with Q = 1 %. The values represented are Mean +/- SEM.

Fixed cell preparation

Cells (C2C12, HEK293T and N2a) were grown to 80% confluence (C2C12 were allowed to differentiate overnight in serum free media). Cells were rinsed, treated as needed, and then fixed with 3% paraformaldehyde and 0.1% glutaraldehyde for 10 min to fix both protein and lipids. Glutaraldehyde was reduced with 0.1% NaBH4 for 7 min followed by three-10 min washes with PBS. Cells were permeabilized for 15 min with 0.2% Triton X-100, blocked with 10% BSA/0.05% Triton/PBS at rt. for 90 min. Primary antibody (PLD2, Cell Signaling #13891; TREK-1, Santa Cruz #sc-50412; PIP_2, Echelon Biosciences #z-P045) was added to a solution of 5% BSA/0.05% Triton/PBS for 60 min at rt at a concentration of 1:100 followed by 5 washes with 1%BSA/0.05% Triton/PBS for 15 min each. Secondary antibody (Life Technologies #A21244 and A21235; cy3B antibodies were produced as described previously(Petersen et al., 2016)) was added in the same buffer as primary for 30 min at rt followed by 5 washes as above. A single 5 min wash with PBS was followed by a post-fix with fixing mixture, as above, for 10 min w/o shaking. This was followed by three-5 min. washes with PBS and two-3 min. washes with dH2O. Cells only receiving CTxB treatment were not permeabilized.

The dual-fixation protocol is used to minimize any effects from post-fixation aberrations. While always good practice for super-resolution in general, this dual fixation also ensures that the movement of any molecule of interest which may not have been immobilized by the initial fixation can be fully immobilized after labeling since the antibodies or toxins used for labeling will be efficiently cross-linked during this post-labeling fixation step. While some have proposed that this problem should be solved by adding the label before the initial fixation(Tanaka et al., 2010) we believe that in the absence of easily-attainable monomeric labeling molecules it would have likely led to clustering artifacts due to the (often) multimeric nature of the labeling proteins.

For cells loaded with cholesterol, 4 ug/mL apolipoprotein E3 (BioLegend, USA) was mixed with fresh 10% FBS and applied to the cells for 1hr prior to shear and or fixing.

Shear force was applied to cells in ibidi μ-Slide $I^{0.4}$ Luer chambers with a flow rate calibrated to apply 3.0 dynes/cm^2. Fixation media (see above) was applied to cells using a syringe pump (Harvard Apparatus PHD ULTRA) and kept at 37°C using an in-line heater (Warner SH-27B).

TREK-1 in HEK293T cells was labeled with a EGFP concatenated to the C-Terminus of full-length human TREK-1 (Fig. S3b), or by applying anti-TREK-1 antibody (sc-398449, Santa Cruz) conjugated to cy3b(Petersen et al., 2016). Anti-PIP_2 antibody was directly conjugate alexa 647 using the same protocol.

Super-resolution dSTORM

Images were recorded with a Vutara 352 and VXL super-resolution microscopes (Bruker Nano Surfaces, Salt Lake City, UT) which is based on the 3D Biplane approach. Super-resolution images were captured using a Hamamatsu ORCA Flash4.0 sCMOS camera and a 60x water objective with numerical aperture 1.2. Data were analyzed by the Vutara SRX software (version 5.21.13 for the data in Figures 3-5 and version 7.0.07 for the data in Figure 2). Single molecules were identified by their brightness frame by frame after removing the background. Identified particles were then localized in three dimensions by fitting the raw data in a customizable region of interest (typically 16 X16 pixels) centered on each particle in each plane with a 3D model function that was obtained from recorded bead data sets. Fit results were stored as data lists for further analysis.

Fixed samples were imaged using a 647 nm and 561 nm excitation lasers, respectively, and 405 nm activation laser in photo switching buffer comprising of 20 mM cysteamine (Sigma, #30070), 1% betamercaptoethanol (BME) (Sigma, #63689) and oxygen scavengers (glucose oxidase, GLOX) (Sigma #G2133) and catalase (Sigma #C40)) in 50mM Tris (Affymetrix, #22638100)+10

mM NaCl (Sigma, #S7653) +10% glucose (Sigma, #G8270) at pH 8.0 at 50 Hz and maximal powers of 647 nm, 561 nm and 405 lasers set to 8, 10, and 0.05 kW cm-2 respectively.

Three-color EGFP-STORM. The dSTORM with EGFP (EGFP-STORM) was performed identical to the two-color dSTORM described above except that a 488 laser was also used to excite EGFP and PIP_2 and CTxB were directly conjugated with fluorescent dyes (Atto 647 and cy3b 555 respectively) obviating the need for fluorescent secondary antibodies. TREK-1 and PIP2 antibodies were conjugated with NHS esters of either Cy3B or Atto 647. 1.5 mg of antibody was conjugated to 3 ng of dye in 1M NaHCO3 buffer pH 8 for 1 hour at room tempurature and separate on a NAP-5 desalting column. The acquisition was performed with no 405-activation laser in GLOX/BME buffer. The GLOX/BME buffer was not required for EGFP blinking, but it did improve the fluorescence and the number of localization particles determined. The resolution TREK-1 localizations determined by EGFP_TREK-1 and cy3b labeled anti TREK-1 antibody were comparable (45-50 nm resolution).

The pair correlation function g(r) and cluster analysis were performed using the Statistical Analysis package in the Vutara SRX software. Pair correlation analysis is a statistical method used to determine the strength of correlation between two objects by counting the number of points of probe 2 within a certain donut-radius of each point of probe 1. This allows for localization to be determined without overlapping pixels as done in traditional diffraction-limited microscopy. For three-color EGFP-STORM probes 1 and 3 and 2 and 3 were also compared using the pair correlation function. Localization at super resolution is beyond techniques appropriate for diffraction-limited microscopy such as Pearson's correlation coefficient. Lipid cluster size was determined using the DBSCAN clustering algorithm also included as part of the Vutara SRX software.

Fluorescence Recovery After Photobleaching (FRAP)

C2C12 cells were grown in DMEM with 10% FBS until 16 hours before use in which they were switched into serum free DMEM. On the day of the experiment, DMEM in live cells was replaced with DMEM w/o phenol red. Fixed cells were rinsed once with PBS and then put into a mixture of PBS with 3% PFA and 0.1% glutaraldehyde for 20 min at 37C. Fixed cells were then rinsed with PBS 5 x 5 min and then placed back into phenol-free DMEM. CTxB (ThermoFisher C34778, 100 ug/ml) was then applied 1:200 into each plate and allowed to incubate for >30 min before imaging. Imaging and data collection was performed on a Leica SP8 confocal microscope with the Application Suite X v.1.1.0.12420. 5 images were taken as baseline after which a selection of 1 or more ROI was bleached at 100% laser power for 6-8 frames. Recovery was measured out to 5 min and fluorescence of the ROI(s) were quantified. The fluorescence before bleaching was normalized to 1 and after the bleaching step was normalized to 0.

Cholesterol Assay

N2a cells were cultured in 48 well plates with 200uL media in each well and then changed to 200uL PBS for the shear treatment. The shear plate was incubated with PBS on an orbital rotator at 3dyn/cm^2 for 10 min in a 37°C incubator. The control plate was incubated with PBS for 10 min in the same incubator with no shear. Then the shear plate was incubated with 200uL 4%PFA+0.1% glutaraldehyde in PBS for 10 min with 3dyn/cm^2 shear and 10 min without shear. The control plate was fixed for 20 min with no shear. Fixed cells were lysed in RIPA buffer (Thermo) and assay in 100 µL PBS with, 4 U/mL cholesterol oxidase, 100 µM amplex red, and 2 U/ml horseradish peroxidase (HRP).

In vitro cellular PLD Assay

In vitro cellular PLD2 activity was measured in cultured HEK293T cells by an enzyme-coupled product release assay(Petersen et al., 2016) using amplex red reagent. Cells were seeded into 96-well plates (~5×10^4 cells per well) and incubated at 37 °C overnight to reach confluency. The cells were starved with serum-free DMEM for a day and washed once with PBS (phosphate-buffered saline). The PLD reaction was initiated by adding 100 μL of reaction buffer (100 μM amplex red, 2 U/ml horseradish peroxidase (HRP), 0.2 U/ml choline oxidase, and 60 μM C8-PC in PBS). The assay reaction was performed for 2-4 hour at 37 °C and the activity was kinetically measured with a fluorescence microplate reader (Tecan Infinite 200 Pro) at excitation and emission wavelengths of 530 nm and 585 nm, respectively. The PLD2 activity was calculated by subtracting the background activity (reaction buffer, but no cells). For the bar graphs, samples were normalized to the control activity at the 120 min time point.

Drosophila Assays

For behavior experiments, 1 to 5-day old flies were collected in vials containing ~50 flies at least 12 hours before the experiment. Flies were allowed to acclimate to behavior room conditions for >30 min (dim red light, ~75% humidity) before each assay. Shock avoidance was tested by placing flies in a T-maze where they could choose between an arm shocking at the indicated voltage every 2 seconds and an arm without shock. Flies were given 2 min to choose which arm, after which flies were collected and counted to determine the shock avoidance index for each voltage and genotype. Control and knockout flies were alternated to avoid any preference and the arm used for shock was also alternated to control for any non-shock preference in the T-maze itself. Shock avoidance index (AI) was calculated as AI= (# flies shock arm-# flies control arm)/# flies total. Plotting the inverse of this metric we obtain a pain sensitivity curve in which we observe a right-shift when the *pld* gene was knocked down (Fig. 3f).

Arousal threshold protocol has been described in detail previously(Murphy et al., 2016). Briefly, animals were exposed hourly to a series of vibrations of increasing intensity ranging from 0.8 to 3.2 g, in steps of 0.6 g. Stimuli trains were composed of 200 ms vibration with 800 ms inter-vibration interval and 15 s inter-stimuli train interval. Stimulation intensity and timing were controlled using pulse-width modulation via an Arduino UNO and shaftless vibrating motors (Precision Microdrives, model 312–110). Arousal to a given stimulus was assigned when an animal (1) was inactive at the time of the stimulus, (2) satisfied a given inactivity criteria at the time of the stimulus, and (3) moved within the inter-stimuli train period (15 s) of that stimulus.

Statistics

All statistical calculations were performed using a student's t-test or Mann-Whitney test in Prism software (v9) unless otherwise noted. For statistics of more than one point along a pair correlation curve a nested Students t-test was used. Significance is noted as follows: ns, $p>0.05$; *$p<0.05$; **$p<0.01$; ***$p<0.001$; ****$p<0.0001$.

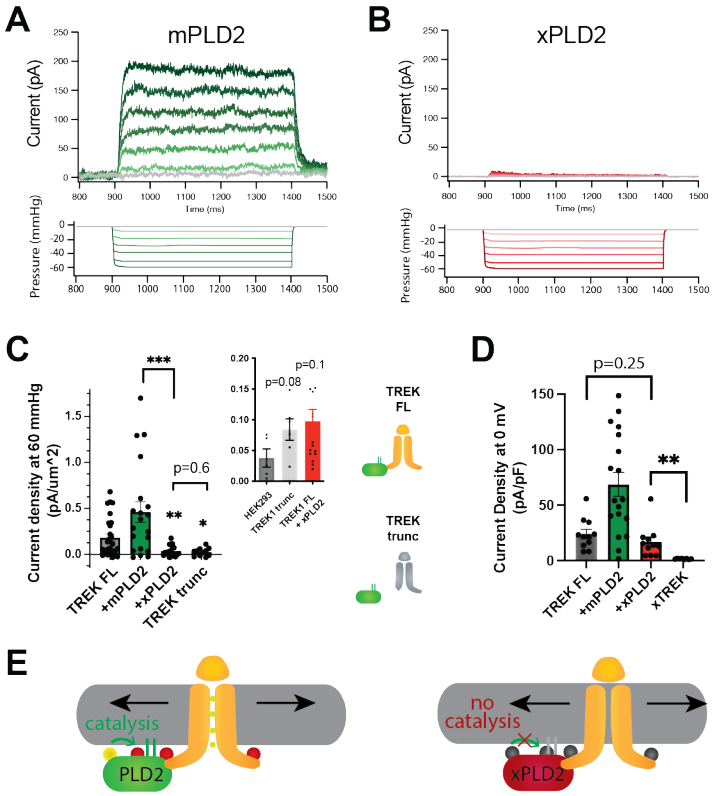

Figure 1. **PLD2-dependent and independent mechanical activation of TREK-1 channels.** (**A-B**) Representative traces from pulled patches of human TREK-1 over expressed in HEK293T cells with mouse phospholipase D2 (mPLD2, green traces) (**A**) or catalytically inactive mouse PLD2 (xPLD2, red) (**B**) under pressure clamp (0-60 mmHg at +30 mV). (**C**) The data, after subtracting HEK293T background current (0.04 ± 0.02 pA/μm^2 n=5 (inset)), are summarized for -60 mmHg. Compared to endogenous PLD2, the expression of xPLD2 eliminated the majority of detectible TREK-1 pressure current ($p<0.007$, n=16-23), as did a functional truncated TREK-1 (TREK trunc) lacking the PLD2 binding site ($p=0.002$, n=15-23). The inset compares mock-transfected HEK293T cells with TREK trunc and full length TREK-1 (TREK FL) + xPLD2, indicative of direct TREK-1 activation. Astricts indicate significance relative to TREK FL, except where noted by a bar. (**D**) Whole cell TREK-1 potassium currents with and without xPLD2. TREK-1 is expressed and functional in the presence of xPLD2. A nonfunctional C-terminal truncation (C321) of TREK-1 (xTREK) is shown with no appreciable current HEK293T cells. (**E**) Cartoon

illustrating PLD2-dependent TREK-1 opening in HEK293T cellular membrane. On the left, membrane stretch (black arrows) mechanically activates PLD2. When PLD2 is active, it makes phosphatidic acid (PA) which evokes the open state of TREK-1. On the right, in the absence of mechanically generated PA, the closed channels remain closed despite the presence of membrane tension . Statistical comparisons were made with an unpaired Student's t test.

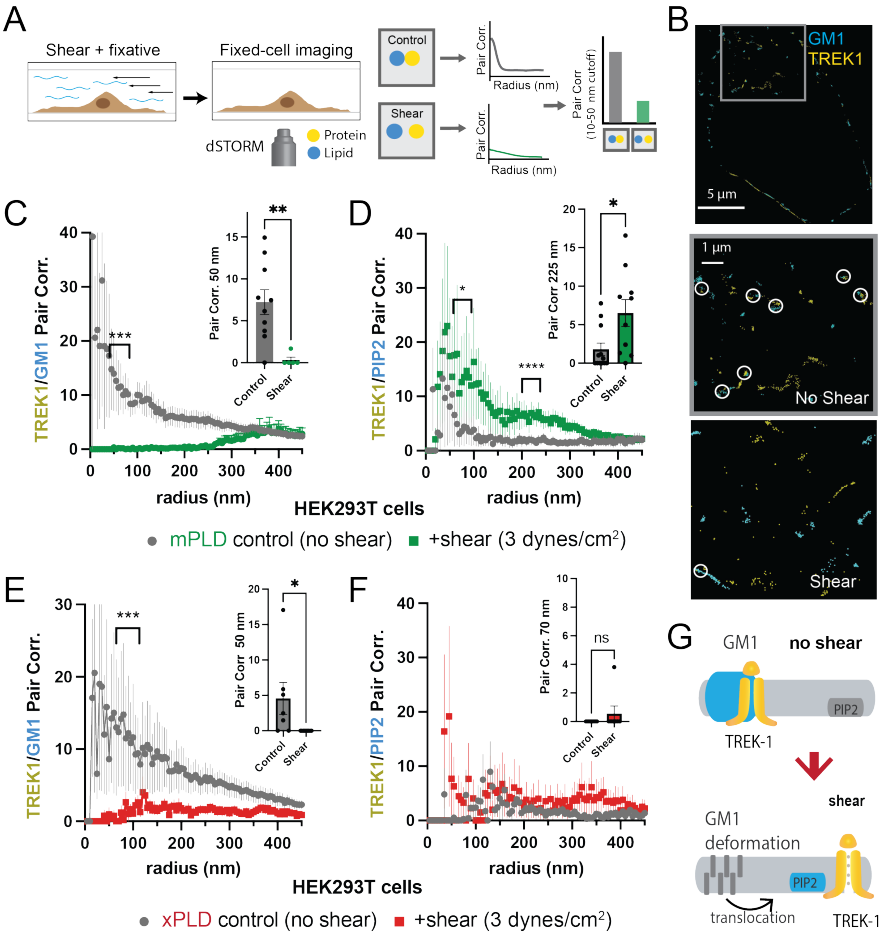

Figure 2 **Shear induces nanoscopic movement of TREK-1 in HEK293T cells.** (**A**) Schematic representation of the shear fixing protocol. Cells grown in a shear chamber are fixed while shear force is applied. Fixed samples are then labeled with fluorescent antibodies or CTxB and subjected to imaging for nanoscopic movement (<250 nm) by two-color super resolution imaging and pair correlation (Pair corr.). (**B**) EGFP-STORM imaging of TREK-1:EGFP and Alexa 647 cholera toxin B (CTxB) with and without shear in HEK293T cells. The middle panel, outlined in grey, is a zoomed portion of the cell surface outlined in the top panel. The bottom panel is a zoomed portion of the cell surface from a cell treated with shear (See Fig. S2I for full image). Locations of TREK-1/GM1 proximity are outlined with a white circle. (**C**) Pair correlation analysis (Pair corr.) of TREK-1 with GM1 lipids before and after shear (3 dynes/cm^2; green) determined by EGFP-STORM imaging when mouse phospholipase D2 (mPLD2) is over expressed (non-

permeabilized). The significance of the Pair corr. change is shown across the range of radii 50-70 nm (along the curve) and at a single 50 nm radius (inset). (**D**) Combined EGFP-STORM imaging of TREK-1 with Alexa 647 labeled PIP_2 in the presence of over expressed mPLD2 (permeabilized). Significance is shown for radii 70-85 nm along the curve and at a single 225 nm radius (inset). (**E**-**F**) Combined EGFP-STORM of TREK-1 in the presence of catalytically inactive PLD2 (xPLD2). Shear (3 dynes/cm^2) of TREK-1 is shown as a red curve with xPLD2 present. The experiments are as described in panels c-d. In (**E**) a significant shift in TREK-1/GM1 Pair corr. is shown for 50-70 nm (along the curve) and at a 50 nm radius (inset). In (**F**) Pair corr. did not appear to shift significantly, as determined by a Student's t-test or for multiple point a nested Student's t-test; *$p<0.05$, **$p<0.01$, ***$p<0.001$, ****$p<0.0001$. (**G**) Cartoon illustrating the association of TREK-1 with GM1 lipids prior to shear (top) and with PIP_2 lipids (bottom) in response to mechanical shear (red arrow).

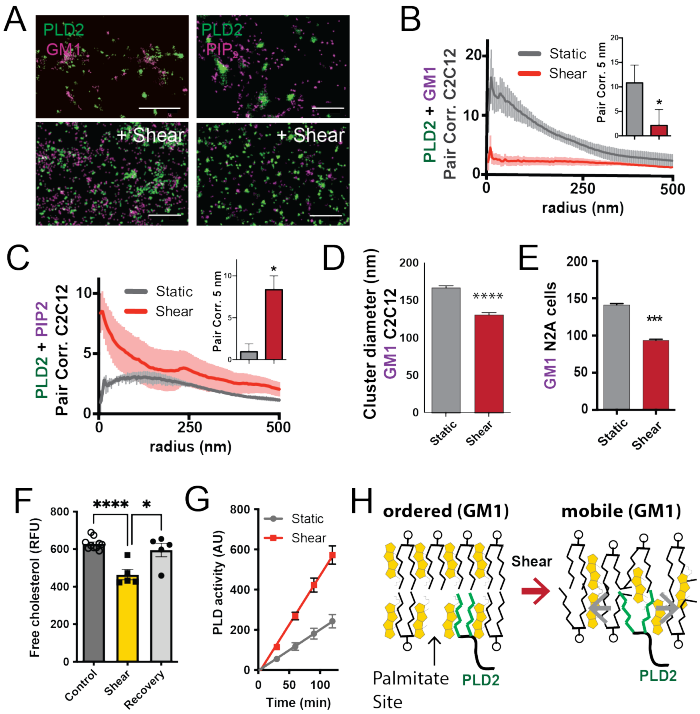

Figure 3. **Shear mobilizes PLD2 within ordered GM1 lipids.** (**A**) two-color dSTORM images of fixed C2C12 cells with and without (3 dynes/cm^2) shear. Cells were labeled with fluorescent CTxB (ganglioside GM1) or antibodies (anti-PIP_2 or anti-PLD2 as indicated) and sheared with the temperature held constant at 37 ℃. Scale bar = 1 μm. (**B**) Pair correlation analysis (Pair corr., unitless) of PLD2 with GM1 or PIP_2 lipids at a given radius. Error bars are displayed at a given radius. A bar graph (inset) is shown at the shortest calculated radius of 5 nm (single point on the x axis). Prior to shear (grey line), PLD2 associates with GM1 clusters; after shear, there is almost no association. (**C**) The opposite was true for phosphatidylinositol 4,5 bisphosphate (PIP_2). Prior to shear, PLD2 does not associated significantly with PIP_2 clusters, after shear, its association increases dramatically. (**D**) Cluster analysis of the GM1 lipids from the C2C12 cells shown in (a). (**E**) Cluster analysis of GM1 lipids in neuroblastoma 2a (N2a) after 3 dynes/cm^2 shear force. (**F**) Fluorescent cholesterol assay. N2a cells grown in a 48 well plates were sheared with 3 dynes/cm^2 orbital fluid shear, fixed with shear (10 min), and compared to control cells with no shear using a fluorescent cholesterol assay. After shear, a second set of control cells were allowed to recover

with no shear and fixative for 30s (recovery), otherwise the cells were treated identical to experimental cells. (n=5-10). (**G**) A live PLD activity assay demonstrates that fluid shear (3 dynes/cm^2) increases substrate hydrolysis in cultured N2a cells. (n>800 clusters from 5-6 cells). (**H**) Depiction of shear thinning activating PLD2. (left) The palmitates of PLD2 (green lines) are shown bound to the palmitate site in ordered GM1 lipids. (right) After shear cholesterol is reduced, and GM1 lipids are deformed. The deformed surface no longer binds palmitates efficiently allowing the palmitates move freely—a process known as shear thinning. Statistical comparisons were made with an unpaired Student's t-test (*$p<0.05$, ***$p<0.001$, ****$p<0.0001$).

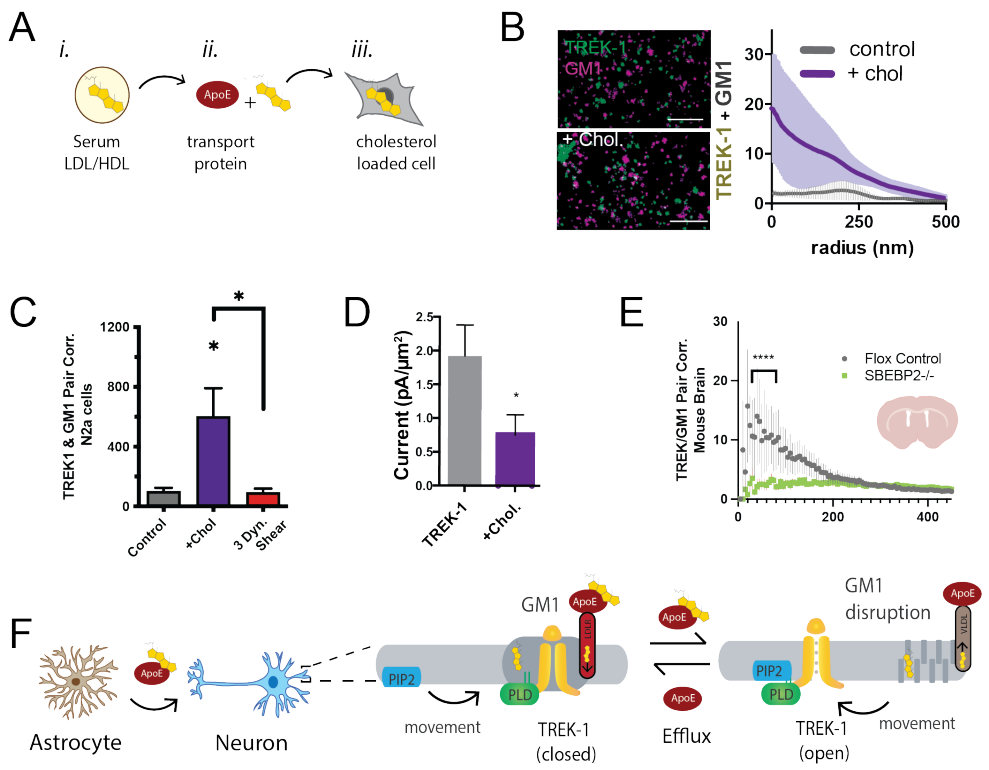

Figure 4. **Astrocyte cholesterol regulates TREK-1 through GM1 lipids and spatial patterning.** (**A**) Uptake of cholesterol into cultured cells using the cholesterol transport protein apolipoprotein E (apoE). (**B**) Cholesterol/lipid uptake into C2C12 cells with 4 µg/ml (~110 nM apoE, purple line). Cholesterol dramatically increases TREK-1 correlation of TREK-1 with GM1 labeled lipids. Without cholesterol (grey line) very little TREK-1 clusters with GM1 lipids. Scale bars = 1 µm. (**C**) Pair correlation (Pair corr.) of TREK-1 and CTxB, localized within 5 nm of each other, are shown plotted after cholesterol treatment (apoE + serum, purple shading) or treatment with 3 dynes/cm^2 shear (red shading)**.** Cholesterol increased TREK-1 association almost 5-fold and shear reversed the effect**.** (n=4-7); unpaired Student's t test (**D**) Current densities from whole cell patch clamp recordings are shown with and without cholesterol loading with 4 µg/ml apoE in HEK293T cells over expressing human TREK-1. Increasing cholesterol inhibited the channel ~3-fold (Student's t-test; *p<0.05) (**E**) Reduction in neuronal cholesterol results in a decrease in correlation between TREK-1 and GM1 cluster in brain slices from a hGFAP-Cre driving the SB2 knockout mouse and its Flox control. Student's t-test at 25nm *p,0.05, nested Students t-test at

25-50 nm (****$p<0.0001$, n=20-24 unspecified cortical regions). (**F**) Proposed model for cluster associated TREK-1 activation and inhibition. In high cholesterol, TREK-1 clusters with PLD2 and ordered (thick) GM1 lipids inhibiting the channel. In low cholesterol, TREK-1 is partially clustered closer to PIP_2 generating basal TREK-1 activity (see also Fig. 1C). After shear, the order of GM1 clusters (dark grey) is disrupted further increasing PLD2 and TREK-1 clustering with PIP_2 lipids (blue).

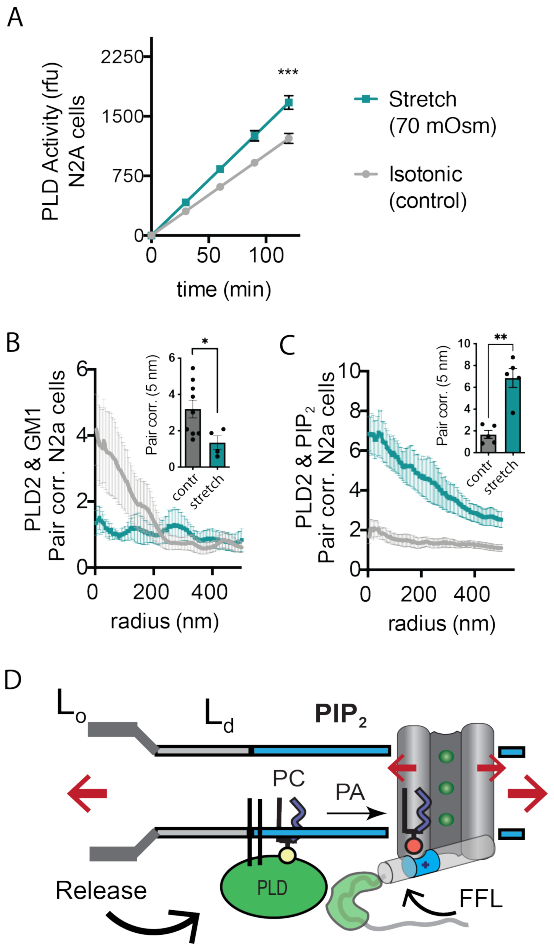

Figure 5. **Osmotic stretch activates PLD2 in N2a cells.** (**A**) Stretch by osmotic swell (70 mOsm buffer) increased PLD2 catalytic activity in live neuroblastoma 2a (N2a) cells compared to isotonic control cells (310 mOsm) (n=5). (**B-C**) dSTORM imaging showing PLD2 trafficking from ganglioside (GM1) to phosphatidylinositol 4,5-bisphosphate (PIP_2) clusters in response to 70 mOsm stretch in N2a cells (coloring the same as in panel **A**. Cells were treated, fixed, and labeled with anti-PIP_2 or PLD2 antibody or cholera toxin B (CTxB, GM1). Prior to stretch, PLD2 clustered with GM1 lipids and very little with PIP_2 (grey lines). After stretch PLD2 clustered robustly with PIP_2 but very little with GM1 lipids. Insets show the change in correlation at 5nm, Student's t-test (n= 5-9), *p<0.05, **p<0.01, ***p<0.001. (**D**) Summary figure for the proposed combined model of TREK-1 in a biological membrane by evoked PLD2-depednent currents and mechanical activation

by direct force from lipid (FFL). TREK-1 in the open conformation (green ions), in complex with PLD2, is shown after stretch (large red arrows) associating (curved black arrow) with PIP_2 clusters (blue shaded bars) in the thin liquid disordered (Ld) region of the membrane (light grey). A known gating helix (grey cylinder) is shown in the up (open channel) position with a PLD2 binding site immediately following the helix (green tube). The opening is a response to three factors that combine to raise the gating helix to the up position. 1) FFL (small red arrows) in TREK-1 favors an open (up) helix conformation. 2) The tip is brought into proximity of PLD2 in the open position and 3) PA (red sphere) is produced and maintains the up positioned by binding to charged residues (blue tube) pulling the helix toward the membrane.

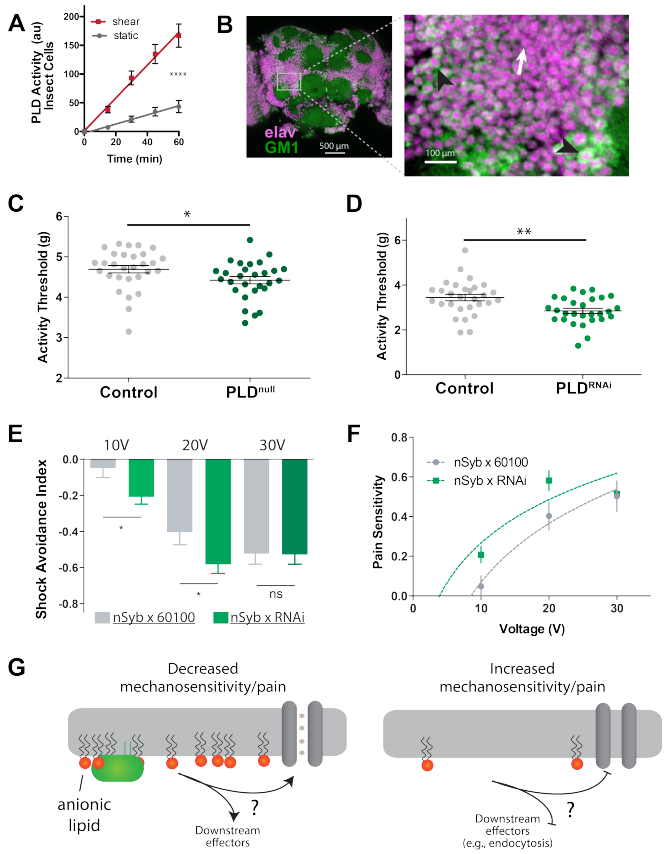

Figure 6. **PLD modulates mechanosensitivity in *Drosophila*.** (**A**) Shear (3 dynes/cm^2) robustly activates PLD2 in a live PLD assay with cultures neuronal insect cells. (**B**) Cholera toxin B (CTxB) robustly labels GM1 lipids (GM1, green), throughout the brain of *Drosophila*. (left). The zoomed section (right) shows that most of the labeling is found on the membrane. There are notable variations in the amount of CTxB labeling, with some cells expressing GM1 over the entire membrane (black arrows) while others only have labeling in small puncta (white arrow). (**C**) Measurements of *Drosophila* mechanosensation *in vivo*. Animals with or without the pld^{null} gene were stimulated by increasing amounts of mechanical vibration (see supplemental Fig. S6). Flies lacking PLD2 had a decreased threshold (i.e., more sensitivity to mechanical stimulation) compared to genetically matched controls (w1118) (p=0.02, n= 28-29), consistent with the prediction that PA decreases excitability of nerves. (**D**) The same result was observed in a PLD^{RNAi} line which results in PLD knockdown only in the neurons of *Drosophila* (p=0.002, n=28-29) Mann-

Whitney test. (**E-F**) Flies were subjected to increasing voltages of electrical shock in a two-choice assay. PLD-KD flies showed an increased sensitivity to shock when compared with wild-type flies. PLD^{RNAi} flies had a higher aversion to shock at 10V (p=0.0213, n=21) and 20V (p=0.0492, n=27-30), but not at 30V (p=0.672, n=12). (**G**) Proposed role of PLD2 in regulating mechanical thresholds. PA is a signaling lipid in the membrane that activates hyperpolarizing channels and transporters. When PA is low the membrane is less polarized, and cells are more sensitive to mechanical activation. The downstream targets are unknown (shown with a '?'). Flies lack a known mechanosensitive TREK-1 homolog.

Supplemental Discussion

In our study, we utilized cholera toxin B (CTxB) and antibody probes for lipid labeling, recognizing that these lipid probes have previously been shown to induce artificial clustering in unfixed cells a phenomenon referred to as “antibody patching”(Moon et al., 2017; Petersen et al., 2020; Veatch et al., 2012). Antibody patching has historically served as a useful tool to segregate proteins within biological membrane, facilitating the determination of their precise localization(Lang et al., 2001; Yuan and Hansen, 2023). In the context of our research, we anticipate that antibody patching might similarly affect lipid distribution, offering a valuable advantage in clearly elucidating the co-localization of proteins with lipids in the membrane.

To address concerns related to potential artifacts stemming from clustering, we adopted a two-step fixation procedure. Initially, cells were fixed during treatment to minimize lipid mobility, followed by a second fixation step after labeling, ensuring fixed antibodies and high localization precision during dSTORM. Additionally, we assessed lipid diffusion after fixing, using our typical experimental protocols. In our system, combined paraformaldehyde and glutaraldehyde effectively inhibited GM1 lipid diffusion, as confirmed by fluorescence recovery after photobleaching (FRAP) experiments conducted in live cells (Fig. S5g-h)).

It is also worth considering potential artifacts arising from variations in labeling density and overcounting, which could impact the size of the lipid clusters analyzed in Figure 3. We quantified the amount of fluorescent labeling (Fig. S5h) and observed a slight reduction in GM1 and PIP_2 labeling after shear, although this change did not reach statistical significance.

The mechanical disruption of PLD2 with GM1 lipids and its association with PIP_2 was determined by the pair correlation function, a method that is robust against artifacts associated with changes in labeling density(Coltharp et al., 2014). Consequently, our data indicating the movement of proteins between domains remains largely independent of potential artifacts

stemming from artificial clustering(Moon et al., 2017; Petersen et al., 2020; Robinson et al., 2019). This conclusion is further supported by the consistency of dSTORM results obtained using both EGFP and cy3b-anti-TREK-1 antibody (Fig. 2, S4).

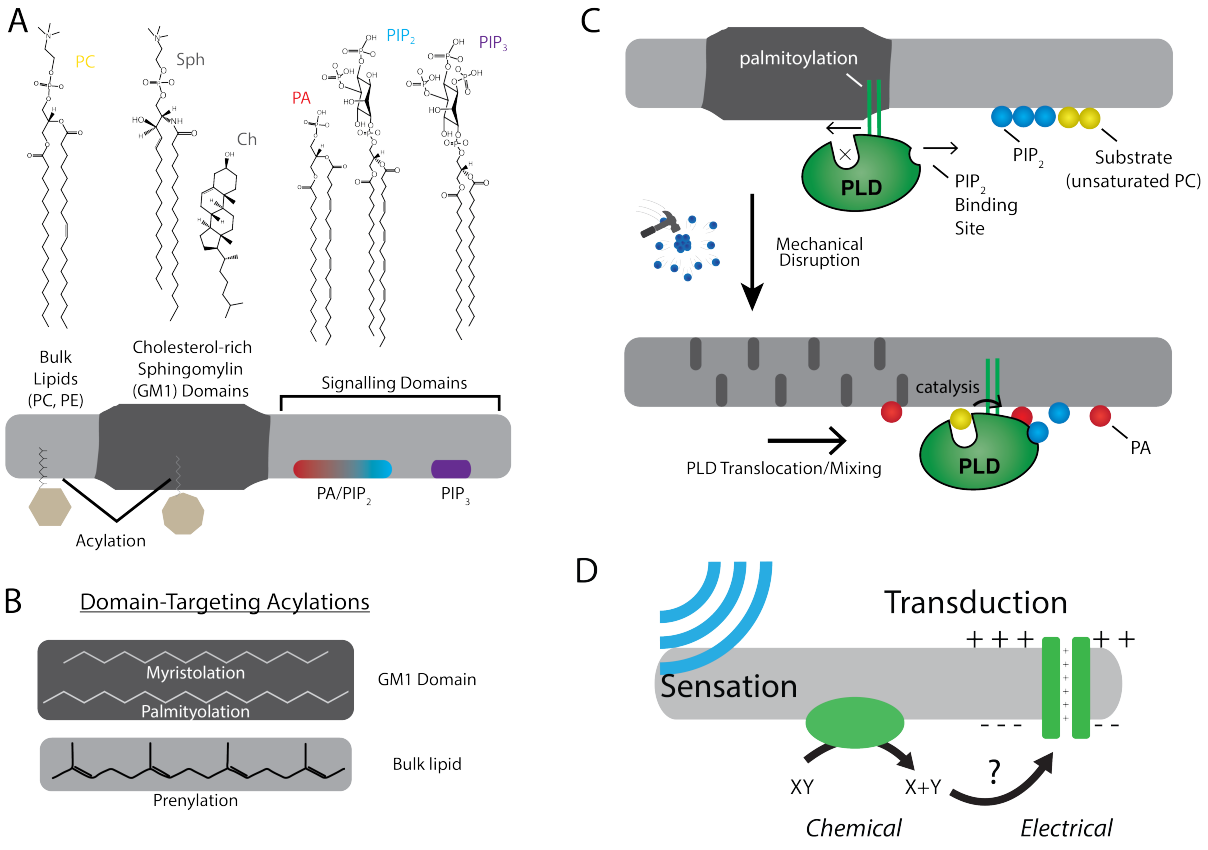

Supplemental Figure 1. **The role of lipids and lipid order in mechano-transduction.** (**A**)The plasma membrane is composed of lipids which can cluster into separate and distinct domains with unique properties such as thickness and charge. Domains for saturated gangliosides (GM1) are shown separate from phosphatidylinositol 4,5-bisphosphate (PIP_2) and phosphatidylinositol 3,4,5 triphosphate (PIP_3). These domains contain proteins which are targeted to the domain through post-translational acylation. (**B**) The types of acylation are shown along with their targeting location. (**C**, top) The enzyme phospholipase D2 (PLD2, green) is shown with its acylation that binds to the saturated ordered site in GM1. The site discriminates palmitoylated proteins from prenylated proteins. This is called the anesthetic/palmitate (AP) site because

anesthetics also compete for this site (not shown)(Pavel et al., 2020; Petersen et al., 2020). (**C**, bottom) Upon chemical or mechanical disruption of the domain, the binding site is disrupted releasing PLD2 from the AP site. PLD2 is then free to bind PIP2 where it has access to its substrate phosphatidylcholine (PC) (**D**) Cartoon depicting a mechanically evoked current through a chemical intermediate.

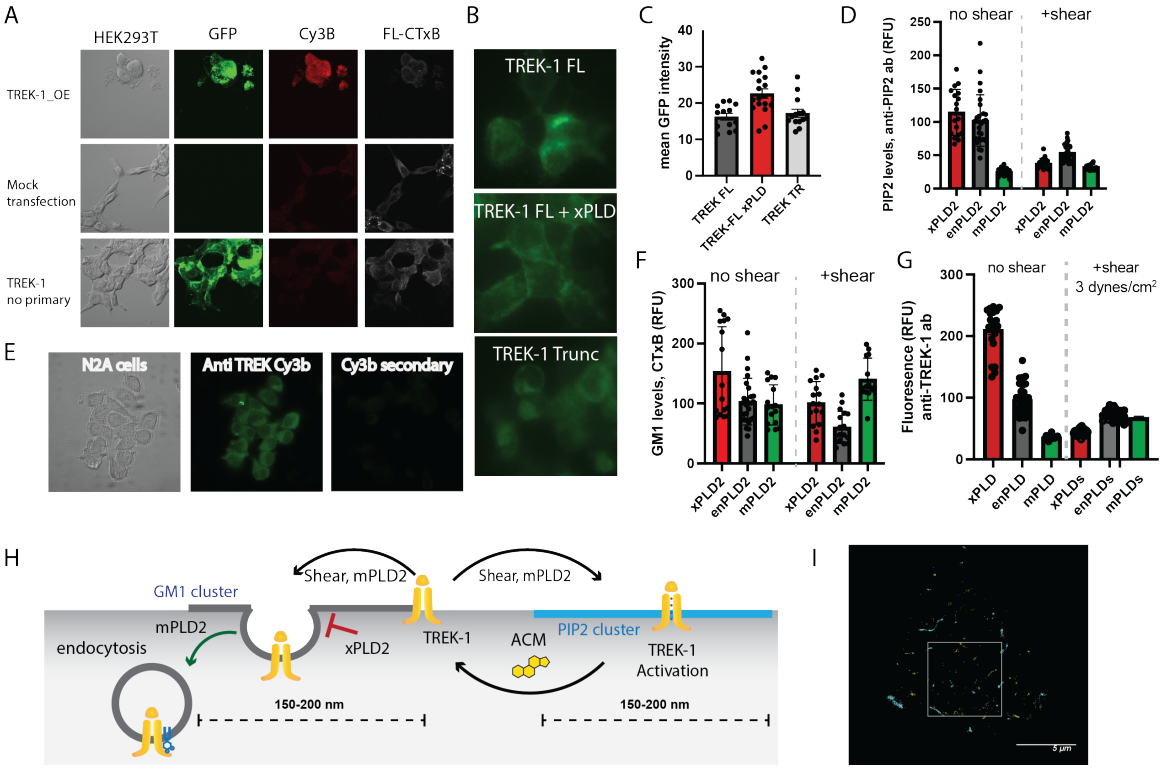

Supplemental Figure 2. **Expression and staining of TREK-1 in cell culture.** (**A**) Confocal images of HEK293T cells overexpressing human TREK-1 tagged with EGFP. The cells were fixed and stained with anti-TREK antibody, a secondary cy3b antibody (red) and A647 conjugated cholesterol toxin B (CTxB, grey) to label lipids. In the absence of transfection, no GFP signal is observed. A negative control, lacking the primary antibody, exhibits no fluorescence. (**B**) Visualization of TREK-1 overexpression in HEK293T cells prepared identical to the cells used for ecophysiology experiments in Fig. (**C**) Overexpression of catalytically inactive PLD2 (xPLD), appears to enhance TREK-1 expression. Truncating the c-terminus (TREK trunc) has no discernible effect on expression TREK-1 at the plasma membrane. (**D**) Shear and overexpression of mPLD2 reduce PIP2 levels on the plasma membrane. (**E**) Immunostaining of endogenous TREK-1 in neuroblastoma 2a (N2a) cells. (**F**) Both mPLD2 overexpression and shear dramatically reduced the amount of GM1 observed by fluorescent staining with cholera toxin B (CTxB). (**G**) Assessment of the impact of shear on TREK-1 levels in HEK293T cells. These cells were

transfected with full-length TREK-1 (TREK FL) and ether xPLD2 or mPLD2. After 24 hours, the cells were subjected to 3 dynes/cm2 rotary shear and fixed. Both PLD2 overexpression and shear resulted in a reduction of TREK-1 expression, likely due to endocytosis processes. (**H**) Cartoon illustrating the role of shear, PLD2, xPLD, in endocytosis. Shear and mPLD2 both activate TREK-1 and decrease TREK-1 surface levels. Presumably the decrease is due to endocytosis since mPLD2 and shear are known to increase endocytosis and xPLD2 is known to block endocytosis. (**I**) dSTORM images showcasing sheared HEK293T cells expressing TREK-1. The image corresponds to the cell depicted in the main Figure 2b. The highlighted box represents an expanded region of this image.

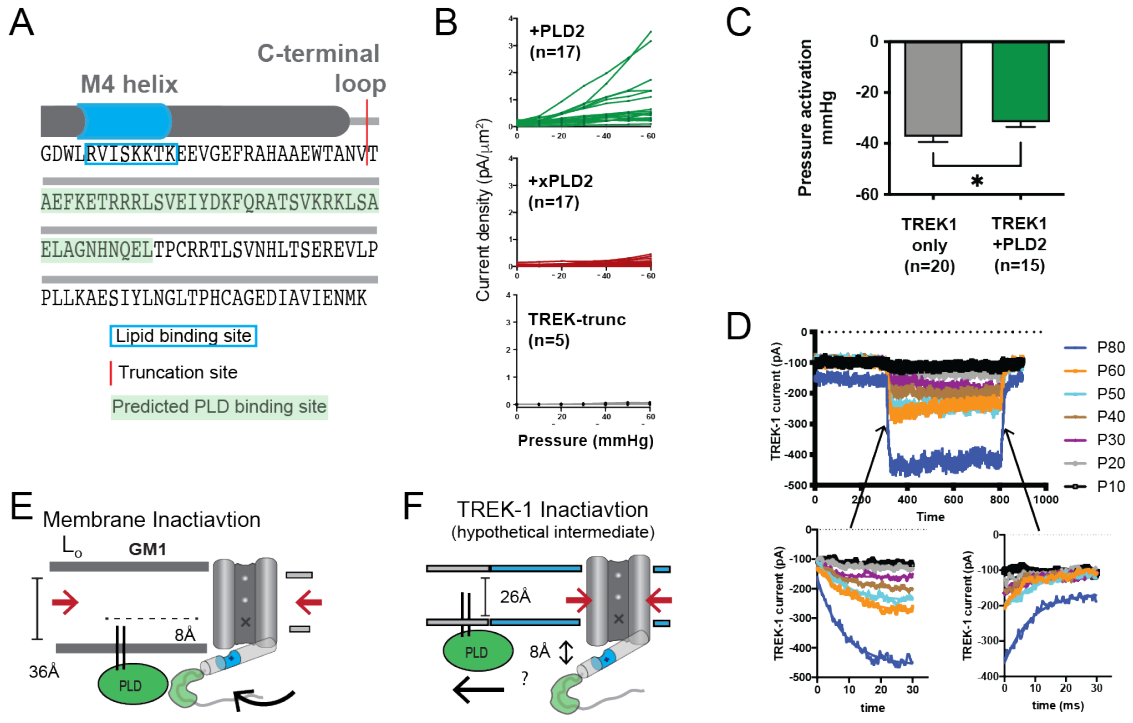

Supplemental Figure 3. **Electrophysiology details and methods.** (**A**) Illustration depicting the C-terminal end of TREK-1. The red region indicates the truncation site used, and the predicted PLD binding site for PLD2 is highlighted. The last transmembrane helix (M4) is depicted as a grey cylinder, and the anionic lipid binding site is highlighted in blue. (**B**) Individual cell traces showing current densities (pA/μm^2) for TREK-1 co-expressed with PLD2 (green), TREK-1 coexpressed with xPLD2 (red), and TREK-1 with a C-terminal truncation (TREK trunc, grey). (**C**) Half maximal TREK-1 pressure current within a non-saturating pressure range of 0-60 mmHg. Overexpression of PLD2 significantly reduces the apparent pressure required to activate TREK-1 ($p<0.05$, n=15-20). (**D**) Representative cell recording displaying TREK-1 pressure currents in response to pressure steps from 0 to 60 mmHg, taken in 10 mmHg increments. The bottom left panel illustrates the activation step and the bottom right panel shows the deactivation. Both activation and deactivation processes appear to occur within sub-5 ms time frames, near the limit of detection for the experimental setup. (**E**) Membrane inactivation process. After mechanical

stretching, the membrane relaxes, allowing the palmitates from PLD2, to re-associate with the GM1 lipids. Consequently, TREK is drawn into GM1 clusters through its interaction with PLD2. In the absence of phosphatidic acid (PA) and due to an increased hydrophobic thickness of the membrane, the channel's gate assumes the down (closed) position, marked with an "X". (**F**) Direct inactivation of TREK-1 through an intermediate. Upon reversal of mechanical stretch (relaxation of the membrane), the channel may transition into a closed conformation due to direct pressure exerted on the channel (indicated by the large red arrows). In a thin membrane this action could displace the gating helix up to 8 Å away from the membrane, disrupting the PLD2/TREK-1 interaction. This putative intermediate state is expected to be transient as TREK-1 would likely re-associate in thicker lipid regions.

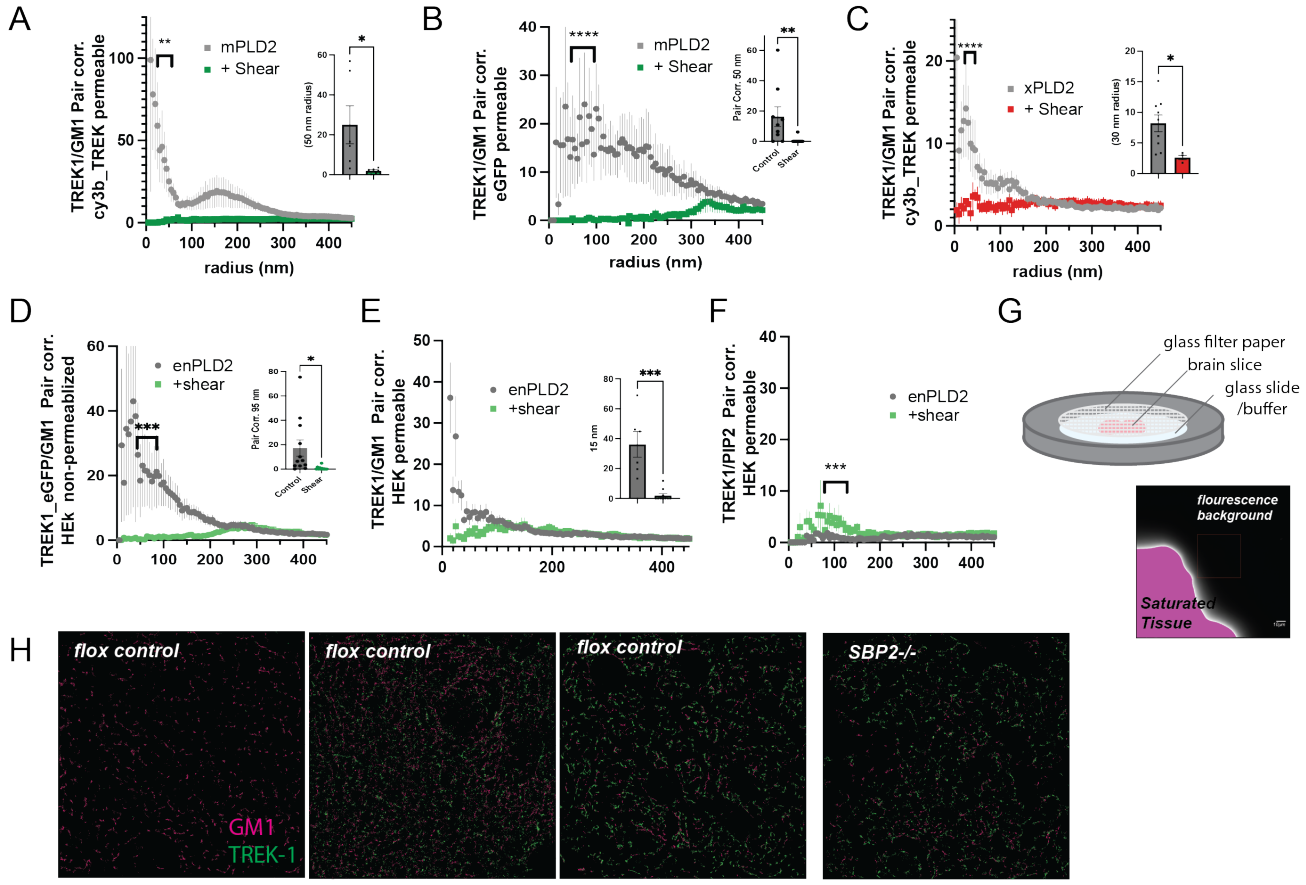

Supplemental Figure 4. **Comparisons of labeling type and permeabilization.** (**A**) Two-color dSTORM using a Cy3b-labeled TREK-1 antibody after mechanical shear in the presence of over expressed mouse PLD2 (mPLD2) and full-length human TREK-1. HEK293T cells were fixed, permeabilized, and stained with a Cy3b-conjugated anti-TREK-1 antibody. Pair correlation (Pair corr.) analysis of TREK-1 with alexa-647-conjugated cholera toxin B (CTxB) was conducted via dSTORM, revealing a decrease in Pair corr. with 3 dynes/cm^2 orbital fluid shear. (**B**) Similar experiments as in panel A, but with Pair corr. analysis from EGFP, which was C-terminally expressed with TREK-1 instead of using a Cy3b-labeled anti-TREK-1 antibody. The use of EGFP in dSTORM buffers resulted in a robust dSTORM signal. This dataset also offers a direct comparison between permeabilized and non-permeabilized cells in Fig. 2B. Pair correlation of TREK-1 with GM1 showed dramatic decreased under three different conditions. (**C**) A comparison of Cy3b-STORM with EGFP-STORM as observed in Figure 2E in the presence of xPLD2. (**D-E**)

A comparison between non-permeabilized (a) and permeabilized (b) HEK293T cells over expressing full-length human TREK-1 (TREK FL) and endogenous PLD2 (enPLD2), i.e., without PLD2 overexpression. Taken from (Call et al., 2023). (**F**) Pair correlation between TREK-1 and PIP_2 increased slightly after mechanical shear. Insets in (a-d) illustrate the variability at a single radius. Statistical analysis for single points was conducted using a Student's t-test, while statistical comparisons at multiple radii were performed with a nested Student's t-test. (**G**) Schematic representation of brain slices prepared for dSTORM. Mouse brains, fixed through whole-body perfusion, were sliced and labeled with Cy3b-anti-TREK-1 antibody and A647 CTxB. These slices were mounted on a cover slip with fiberglass filter paper on top to secure the tissue during imaging with dSTORM buffer added to the filter paper. The fluorescent background (640 nm) was undetectable even at saturating light intensities. (**H**) Example images of brain slices from control and astrocyte specific SREBP2 null mice. TREK-1 was expressed in most brain regions but not uniformly (left panel). Pair correlation analysis was performed on regions with both TREK-1 and CTxB labeling. The displayed slice is a coronal section near the hippocampus, although the precise region of interest is unspecified. Significance was determined by a Student's t-test for a single point. For multiple points a nested student's t test was used (*$p<0.05$, ** $p<0.01$, *** $p<0.001$, ****$p<0.0001$).

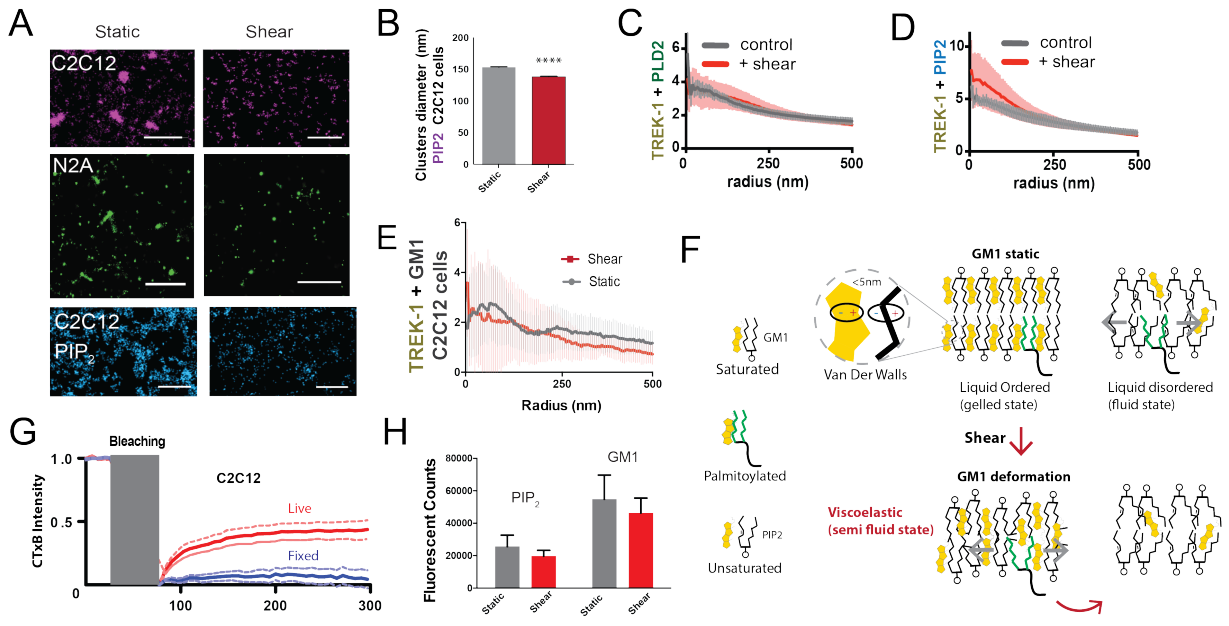

Supplemental Figure 5. **Observing cellular changes in response to mechanical stimulation**. (**A**) Representative images illustrating the impact of shear on the apparent size of GM1 (maroon and green) in muscle C2C12 and neuronal N2a cells respectively. PIP_2 clusters in C2C12 cells are shown in blue. When shear force is applied the apparent size decreases. Scale bars = 1 µm. (**B**) Cluster analysis of PIP_2 demonstrates a small but statistically significant decrease in size. (**C**) Complex formation between TREK-1 and PLD2 before and after shear in C2C12 cells. Pair correlations analysis of TREK-1 and PLD2 before (grey line) and after (red line) 3 dynes/cm^2 shear. Their association remains almost identical in both states. (**D**) Staining of TREK-1 with phosphatidylinositol 4,5 bisphosphate (PIP_2) antibody in C2C12 cells. Before shear (grey line) TREK-1 exhibits significant association with PIP_2. After shear, this association further enhanced, suggesting some TREK-1 complexes move to PIP_2 clusters in C2C12 cells. (**E**) Pair corr. of TREK-1 with GM1 clusters (CTxB) measured by dSTORM in C2C12 cells prior to cholesterol loading, as shown in Fig. 4b. In the low cholesterol state, endogenous TREK-1 shows minimal association with GM1 lipids. (**F**) Shear thinning model for PLD2. Cholesterol is depicted as packing with saturated lipids and saturated palmitate via Van der Waals interactions (within 5 nm). Unsaturated lipids contain a double bond that alters the packing surface of a lipid. In a perfectly

ordered state, palmitoylated proteins are ordered with the GM1 lipids and cholesterol. In the disordered region palmitates move fluidly within the membrane. After shear the GM1 lipids remain ordered but deformed. The palmitates no longer efficiently pack with the GM1 lipids, reducing their affinity for the ordered domain and allowing the palmitates to move in the membrane. (**G**) Fluorescence recovery after photobleaching (FRAP) imaging to examine potential labeling artifacts(Moon et al., 2017; Raghunathan and Kenworthy, 2018; Wang et al., 2018) of pentavalent CTxB that might persist after fixation. The duration of photo bleaching is indicated in grey. The blue line shows that fixation with paraformaldehyde (PFA) and glutaraldehyde effectively restricts the large-scale movement of lipids in fixed cells compared to live cells (red). (**H**) For both PIP_2 and GM1 labeling, shear did not significantly decrease the overall counts measured with dSTORM in C2C12 cells ($p > 0.05$, Student's t-test).

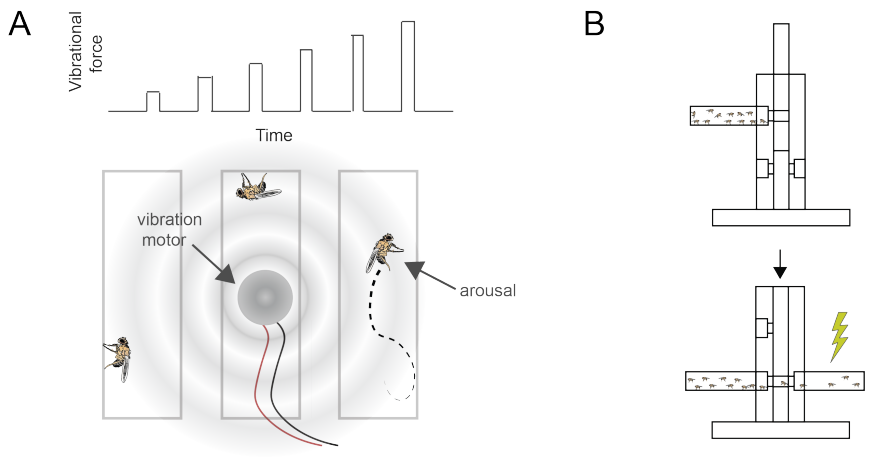

Supplemental Figure 6. **Pan-neuronal knockdown of *pld* in Drosophila alters sensitivity to electrical shock**. (**A**) Demonstrates that PLD activity in neuroblastoma 2a (N2a) cells increases in response to mechanical force. (**B**) Illustration of the experimental setup for applying mechanical stimulation to Drosophila flies. A series of six increasing vibrations (top) used to stimulate the flies. A vibration motor was attached to the back of the chamber containing the flies, and their responses were monitored using a web camera to assess stimulation-induced arousal (bottom).

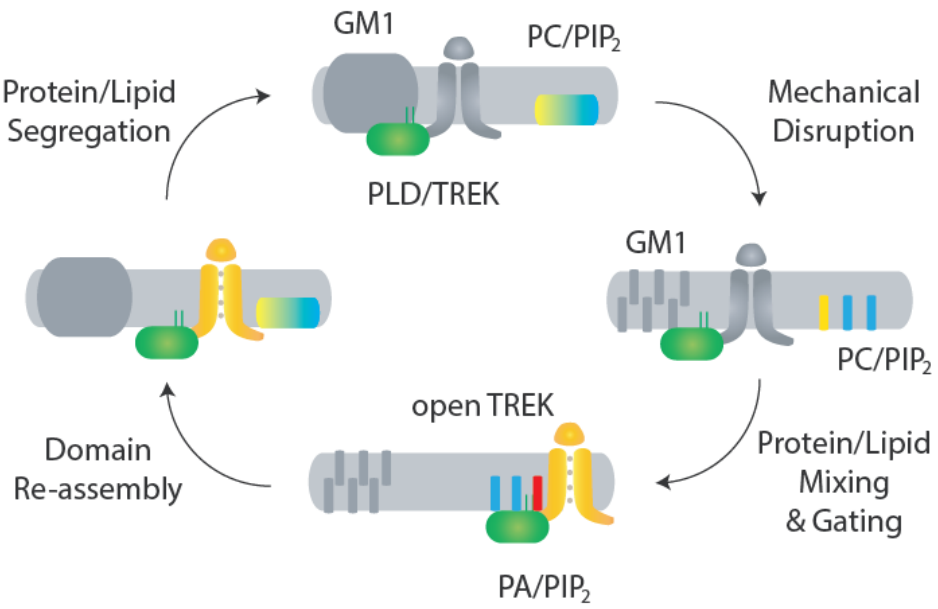

Supplemental Figure 7. **Proposed model for domain-mediated mechanosensation of TREK-1 by spatial patterning**. (top) In domain-mediated mechanosensation, in an unstimulated state, the palmitate site within GM1 domains is intact and binds tightly to palmitates. This tight affinity sequesters the PLD2/TREK-1 complex away from its activating lipids phosphatidylcholine (PC, yellow) and phosphatidylinositol 4,5-bisphosphate (PIP_2, blue). (right) Upon mechanical stimulation, the palmitate site is disrupted and the PLD2/TREK-1 complex is released, allowing it to diffuse within the plasma membrane and bind to PIP_2. (bottom) Upon PIP_2 binding, PLD2 is becomes activated and makes phosphatidic acid (PA, red), transducing the mechanical signal into a chemical signal. This chemical signal then binds to and activates TREK-1, initiating chemical-to-electrical signal transduction. (left) When the stimulation is removed, the lipid domain reforms, causing the complex to be re-sequestered. The process results in a return to steady-state conditions, as depicted in the top panel